International Journal of Plasticity 188 (2025) 104294

Contents lists available at ScienceDirect

International Journal of Plasticity

journal homepage: www.elsevier.com/locate/ijplas

The quantitative evaluation of the plasticity of Nb/amorphous CuNb nanolayered thin films by micro-pillar compressions and micro-indentations as well as their correlation

Feng Qin [a,b], Yaodong Wang [c], Jie Chen [a], Shaohua Chen [d], Jianjun Li [a,b,*]

[a] *College of Mechanical and Electrical Engineering, Central South University, Changsha 410083, Hunan, PR China*
[b] *State Key Laboratory of Precision Manufacturing for Extreme Service Performance, Central South University, Changsha 410083, Hunan, PR China*
[c] *School of Mechanics and Civil Engineering, China University of Mining and Technology, Xuzhou, Jiangsu 221116, PR China*
[d] *School of Aerospace Engineering, Beijing Institute of Technology, Beijing 100081, PR China*

ARTICLE INFO

Keywords:
Nanolayered thin films
Plasticity
BCC crystalline/amorphous interface
Micro-pillar compression
Micro-indentation
Shear banding

ABSTRACT

Micro-indentation (MI) tests have been widely used to investigate the deformation of nanolayered metallic films (NMFs) due to the convenience, simplicity and low cost. However, MI is unable to directly provide a quantitative information on the plasticity of the NMFs because of the complex 3-D stress state. Here, a combinational approach is proposed to address the above critical issue, in which systematic micro-pillar (MC) tests has been first conducted to investigate the strength and plasticity of Nb/amorphous CuNb NMFs with layer thicknesses of 100 nm, 40 nm and 5 nm. Then, an effective strain based theoretical model has been developed to derive a homogeneous deformation strain (HDS) by distinguishing the shear banding-induced strain localization region from the non-localized one for the MI-induced 3-D stress state. The MI-derived HDS can be directly compared with the MC-measured one that is determined as the maximum applied strain without causing shear banding and micro/nano-cracks in the deformed pillars. The results show that the MI-evaluated HDSs are in quantitatively agreement with the MC-measured ones, revealing the best plasticity (i.e., with HDS of 48.5 %) in the 40 nm sample. The enhanced plasticity in the 40 nm sample is attributed to the deformation twinning in the Nb layers as revealed by the transmission electron microscopy analysis and molecular dynamics simulations. The above findings demonstrated that the plasticity of NMFs can be quantitatively evaluated by several simple MI tests with the aid of the developed combinational approach, in which the time-consuming and costly MC tests could be avoided.

1. Introduction

Nanocrystalline metals and metallic glasses (MGs) usually exhibit remarkable strength but limited ductility (Kou et al., 2014; Lyu et al., 2017; Ma and Zhu, 2017; Ovid'ko et al., 2018; Schuh et al., 2007; Wang et al., 2023; Wu and Fan, 2020). For the former, the failure occurs via the crack nucleation and shear instability during mechanical loading due to their low strain hardening capacity, which results in a low tensile ductility of a few percent of applied strain (Meyers et al., 2006). MGs typically show macro-brittleness

---

[*] Corresponding author at: College of Mechanical and Electrical Engineering, and State Key Laboratory of Precision Manufacturing for Extreme Service Performance, Central South University, Changsha 410083, Hunan, PR China.

E-mail addresses: mejjli@csu.edu.cn, jianjunli.mech@hotmail.com (J. Li).

https://doi.org/10.1016/j.ijplas.2025.104294
Received 24 January 2025; Received in revised form 4 March 2025;
Available online 8 March 2025

failure with near zero tensile ductility at ambient temperature conditions, originating from the strong tendency with severe strain localization in the form of shear bands (SBs) (Chen et al., 2013; Greer et al., 2013). The SB generally originates from the condensing of shear transformation zones along a viable shear path, which propagates instantly under applied stress and leads to strain softening of materials, as revealed by experimental (Jang and Greer, 2010), theoretical (Jiang and Dai, 2009; Jiang et al., 2020) and simulation studies (Li et al., 2023; Sha et al., 2017; Yuan and Branicio, 2020). Interestingly, unexpected tensile ductility of 4–14 % has been achieved by combining the nanocrystalline and amorphous metals via layered structure design, without sacrificing the original high strength of the constituent phases (Fan et al., 2017a; Kim et al., 2011; Wang et al., 2007). For example, by using magnetron sputtering, Wang et al. (2007) fabricated a crystalline/amorphous layered composite by alternately stacking 35 nm Cu and 5 nm amorphous CuZr layers. Their subsequent tensile tests revealed a high flow strength of 1.1 GPa with exceptional elongation (∼ 14 %) in this composite, which was much higher than the nanocrystalline copper (< 2 %) (Wang et al., 2007). The excellent tensile ductility was attributed to the high capacity of the amorphous layer as dislocation sources and sinks that accommodate the plasticity of the crystalline layer (Wang et al., 2007). Moreover, high thermal stability (Russell et al., 2024), enhanced fracture toughness (Wang et al., 2015) and radiation damage tolerance (Schuler et al., 2020) were also reported in crystalline/amorphous composites, enabling them as candidates for multifunctional applications in micro and nano-electromechanical systems.

Layer thickness is one of the most important microstructural parameters for multilayered composites, which plays a key role in determining the mechanical properties and the deformation mechanism (Chen et al., 2020b; Jian et al., 2022; Li et al., 2016; Su et al., 2021; Wu et al., 2023b), e.g., the pronounced size effect between strain localization and layer thickness as reported in Ni/Ni-W (Liang et al., 2024) and Cu/Nb (Dong et al., 2020) layered composites. To date, extensive studies have focused on layer thickness-dependent mechanical behaviors of the face-centered cubic (FCC) crystalline/amorphous nanolayered metallic films (NMFs), such as Cu/CuZr (Cui et al., 2015; Guo et al., 2014; Zhang et al., 2012c), Cu/CuNb (Fan et al., 2017a, 2016), Cu/PdSi (Knorr et al., 2013), etc. For FCC crystalline/amorphous NMFs, the tendency of shear banding (shear instability) increases as layer thickness decreases or the amorphous layer thickness increases as demonstrated both by micropillar compression (Guo et al., 2014; Knorr et al., 2013; Zhang et al., 2012c) and nanoindentation (Cui et al., 2015). For instance, Zhang et al. (2012c) showed that the deformation of the Cu/amorphous CuZr NMFs transmitted from a stable plastic deformation accompanied by the extrusion of the softer Cu layer to a shear banding deformation as the layer thickness decreased from 100 nm to 10 nm as examined by micropillar compression. Similarly, the increased shear banding behaviors with the reduction of the layer thickness were also reported in crystalline/crystalline NMFs under nano-/-micro-indentations (Li et al., 2010b; Wang et al., 2011).

As compared to the well-studied FCC crystalline/amorphous NMFs, there are only a few studies on the NMFs with body-centered cubic (BCC) crystalline phase (Chou et al., 2011; Gu et al., 2017; Wang et al., 2018). For example, Chou et al. (2011) introduced the high-stiffness BCC Ta phase (with Young's modulus of 200 GPa) to combine with an amorphous CuZrTi phase, aiming to simultaneously achieve high strength and high plasticity in crystalline/amorphous NMFs. They found that the yield strength of the fabricated 50 nm CuZrTi/Ta film reached as high as 3.2 GPa, which is 87 % higher than that of the monolithic amorphous CuZrTi phase. However, the deformations of the CuZrTi/Ta films and the monolithic amorphous CuZrTi alloy are both governed by severe shear banding that appears at a small applied strain (below 0.2 %) under micropillar compression, resulting in a low failure strain of ∼0.5 % for the former and ∼0.4 % for the latter. In addition to the thickness of the constituent layers, the thickness ratio (η) of the amorphous to crystalline layers has a significant influence on the mechanical properties of crystalline/amorphous NMFs. For instance, Wang et al. (2018) reported that the tensile ductility of BCC Mo/amorphous CuZr NMFs is monotonically increased with increasing η. However, the fracture behavior exhibits the typical brittle mode and is independent of the η parameter. This brittleness of the Mo/CuZr film was ascribed to the initiation of microcracks in the brittle Mo nanolayer and the limited plasticity of the amorphous CuZr layer. The aforementioned studies clearly show that the deformability of the crystalline/amorphous NMFs with a brittle BCC crystalline (e.g., Ta and Mo) is extremely limited, although the films can be highly strengthened.

Typically, micropillar compressions (MCs) and nano-/micro-indentations (MIs) are the common techniques to characterize the microscale mechanical response of materials, such as the size effects of NMFs (Cao et al., 2019, 2021; Chen et al., 2020a; Cheng et al., 2024; Feng et al., 2017; Li et al., 2017, 2022, 2008; Liu et al., 2013; Mayer et al., 2016) and MGs (Jang et al., 2011; Jiang et al., 2020; Yoo et al., 2012) because it is still a challenge to perform microscale tensile testing due to the difficulty in preparing the small-scale dog-bone specimen and in fabricating the specimen holding device and stress–strain measurement for thin film samples (Hemker and Sharpe, 2007; Rajagopalan et al., 2007). Recently, the authors discovered a non-monotonic shear banding-mediated strain localization in BCC Nb/amorphous CuNb NMFs with decreasing layer thickness from 100 nm to 2 nm by MI tests (Qin et al., 2024), which results in an optimal layer thickness of 40 nm that produces a homogeneous deformation since the severe shear banding as observed in the samples with larger layer thickness (100 nm, 65 nm) and smaller layer thickness (20 nm to 2 nm) under a load of 50 g has been completely suppressed. This special non-monotonic shear instability behavior is only observed in the designed BCC Nb/amorphous CuNb NMFs, which is in clear contrast to the monotonically increased shear instability in all other layered systems such as FCC-FCC (Cu/Au (Li et al., 2010b), Cu/Ag (Wen et al., 2007)), FCC-BCC(Cu/Ta (Wang et al., 2011), Cu/Cr (Li et al., 2011)), etc.

However, at present, it is unlikely to quantitatively evaluate the plasticity of NMFs by simple MI tests due to the indentation-induced complex 3-D stress state. Yet, MC testing is a powerful tool that has been widely used to achieve the above goal by providing stress–strain responses due to the deformation-induced simple uniaxial stress state, which can be employed to get the yield strength and strain hardening behavior (Cao et al., 2019, 2021; Zhang et al., 2012a, 2012c). Hence, the fracture strain, micro-crack initiation strain, the corresponding microstructure evolution and the flow stress can be directly obtained. These critical parameters cannot be given in the MI tests. Unfortunately, the MC tests are much more difficult to conduct, e.g., the pillar preparation, the pillar compression tests, and the TEM lamella preparation for the deformed pillars require elaborate operations and hence are much more time-consuming and costly, as compared with the simple MI tests. In addition, it is noted that the deformation and fracture behaviors under MC-induced isostress state are totally different from those under MI-produced 3-D stress state. For example, a heterogeneous Cu/Zr NMF shows a homogeneous deformation up to ~30 % strain without shear banding and interface failure under MCs (e.g., interface sliding typically indicated by significant extrusion of the soft layer) (Li et al., 2020). However, severe shear instability still occurs in the same sample by forming multiple SBs under MIs with a load of 500 mN (Li et al., 2022). Similarly, a 100 nm Cu/amorphous CuZr NMF exhibits a homogeneous deformation under MCs with the applied strain of ~20 % (Guo et al., 2014), whereas cutting-like SBs were observed in this sample under MIs with a load of 250 mN (Guo et al., 2015).

Therefore, the objective of the present work is to answer the following critical questions: (i) Can the plasticity of the thin film samples be quantitatively measured by MI tests? (ii) is the plasticity of the thin film samples measured by the MIs that generate a complex 3-D stress state consistent with that by the MCs that produce an isostress state? (iii) why does the Nb/amorphous CuNb NMF with layer thickness of 40 nm possess the best plasticity as compared with the other samples with larger or smaller layer thicknesses? Here in this work, an attempt has been made to address the above important issues. First of all, systematic MC tests have been conducted to investigate the mechanical behavior of the three typical Nb/amorphous CuNb samples with layer thickness of 100 nm, 40 nm and 5 nm, respectively. The yield strength, strain hardening, micro-crack initiation strains, and deformation mechanisms are presented and discussed with the aid of high-resolution transmission electron microscopy (TEM) characterizations of the deformed pillars, finite element (FE) and molecular dynamics (MD) simulations. Secondly, the previous theoretical model (Qin et al., 2024) has been extensively extended here by incorporating the 3-D stress state in order to develop an effective strain-based approach to give a quantitative correlation between the MC-derived plasticity and the MI-measured one. In the refined theoretical model, the pure shear stress state assumption has been abandoned, while the 3-D stress state is incorporated to give a more real representation for the deformation state under MIs. The paper is organized as follows. The experimental details are given in Section 2. Section 3 presents the MC and MI-induced deformation behavior and mechanism of the Nb/amorphous CuNb NMFs as well as the newly-proposed approach. The conclusions are made in Section 4 with the discussion of the possible limitations of the developed theoretical model and the likely improvement of the model.

2. Materials and methods

2.1. Material preparation

The Nb/amorphous CuNb NMFs were prepared by magnetron sputtering (PTL6S PVD system) with alternately depositing Nb and amorphous CuNb layers on Si (100) wafers. The Nb layer was synthesized by sputtering the Nb target (purity of 99.95 %), whereas the amorphous CuNb layer was realized by co-sputtering the Nb and Cu (purity of 99.99 %) targets. The first layer was Nb while the top layer was amorphous CuNb. The base vacuum pressure was 5 × 10^{-5} Pa while the deposition pressure was 0.3 Pa with high pure Ar gas

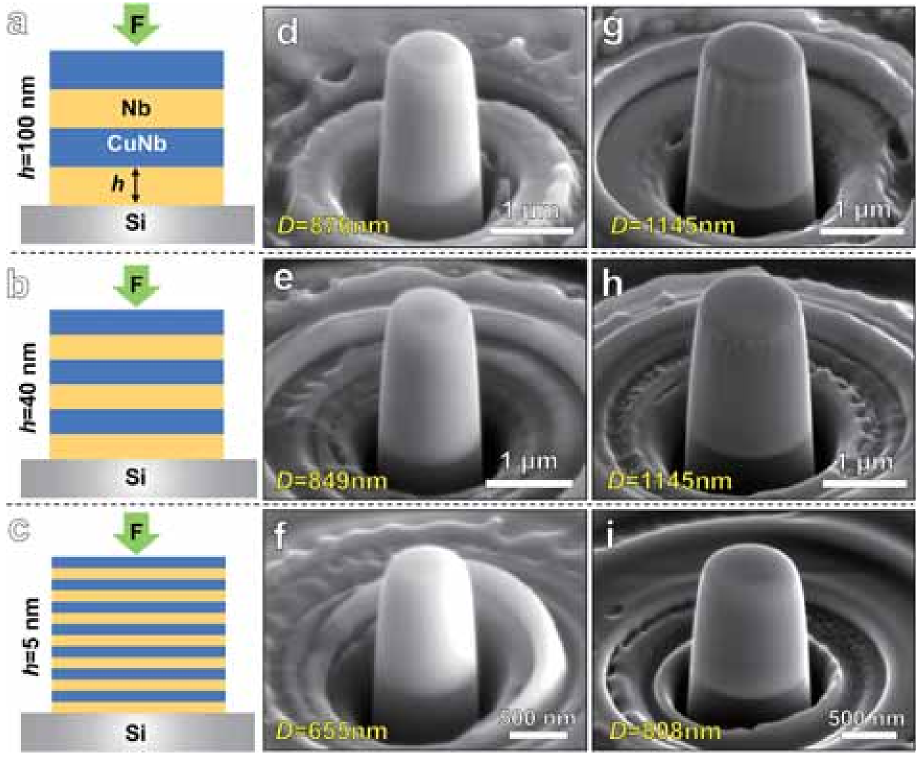

Fig. 1. (a–c) Schematic of the MC tests for the BCC Nb/amorphous CuNb NMFs with h = 100 nm, 40 nm and 5 nm. The loading direction is perpendicular to the layer interface. (d-i) Representative 52°-tilted SEM images of the as-prepared (d-f) small and (g-i) large pillars for the three samples, i.e., h = (d, g) 100 nm, (e, h) 40 nm and (f, i) 5 nm, where "D" designates the pillar diameter.

(99.999 wt %). The powers applied for Cu and Nb targets were 67 W and 150 W, respectively. The above settings produced a deposition rate of 0.1355 nm/s for the Cu target and 0.1379 nm/s for the Nb target, which yields the atomic molar ratio of 3:2 for Cu and Nb atoms in the amorphous CuNb layer. Three film samples with individual layer thicknesses (h) of 100, 40 and 5 nm were prepared, and the corresponding sample thicknesses were 1.88, 1.84 and 1.15 μm, respectively.

2.2. Mechanical tests

To investigate the mechanical performance of the Nb/amorphous CuNb NMFs under the uniaxial stress state, a series of MC tests were performed in the present study. The loading direction was perpendicular to the layer interface, as illustrated in Fig. 1a–c. Micropillars were prepared by focused ion beam (FIB) milling (FEI Helios Nanolab 600i) at 30 kV by decreasing the outer and inner diameters of a series of circle patterns. The final milling voltage/current was 30 kV/18 pA to minimize the pillar taper. For each sample, a series of large and small pillars were prepared to explore the potential extrinsic size (pillar diameter) effect on the mechanical properties. The average diameters (D) of the as-prepared large pillars were 1087 ± 75 for the 100 nm sample, 1146 ± 32 nm for the 40 nm sample and 768 ± 50 nm for the 5 nm sample, which are significantly larger than those of the small ones, i.e., 846 ± 45 nm for the 100 nm sample, 853 ± 15 nm for the 40 nm sample and 645 ± 23 nm for the 5 nm one. Besides, MCs were also conducted for the monolayer amorphous $Cu_{60}Nb_{40}$ and Nb film samples for comparison. The average diameter of the pillar for the $Cu_{60}Nb_{40}$ monolayer sample was 596 ± 44 nm while that of the Nb monolayer sample was 644 ± 51 nm. The aspect ratio (height/diameter) of the prepared pillars was ~1.5–2, and the taper of each pillar was less than 5°. The representative as-prepared pillars for $h = 100$ nm (Fig. 1d, g), 40 nm (Fig. 1e, h) and 5 nm (Fig. 1f, i) samples are shown in Fig. 1. MC tests were performed by using the Keysight Nano Indenter G200 with a 10 μm-diameter diamond flat punch under the load-control mode. Generally, a typical loading rate between 0.8 and 100 μN/s has been recommended for the MC test to achieve a quasi-static loading when using the load-control mode in a nanoindenter system (Volkert and Lilleodden, 2006). Here the applied loading rate was set to be 10 μN/s, which was sufficiently small to achieve a quasi-static loading, avoiding unveracious high flow stress and homogeneous deformation that usually occur in MC tests (Dehm et al., 2018). The allowable drift rate was controlled below 0.1 nm/s and corrected automatically during load–displacement data acquisition. At least 6 times independent MC tests were conducted for each sample with small or large pillars. The MI study on the same samples has been conducted in our previous work (Qin et al., 2024), in which the MI tests were carried out at room temperature by using a Vickers indenter (Shimadzu HMV-G20ST) and six MI tests under an applied load of 50 g with 5 s holding time were performed for each sample.

It should be noted that the stress state under MCs may change from a uniaxial stress state to a 3D-one when the pillar is deformed to a barreling/bulge shape. Hence a purely axial loading might be corrupted. The main reason is that there exists friction between the flat punch indenter and the pillar top surface, which causes lateral forces that can ruin the uniaxial stress state in the pillar (Dehm et al., 2018). However, the magnitude of lateral forces does not only depend on the friction coefficient but also on the lateral compliance of the used indenter system, which is mostly unknown or hard to determine. Therefore, in order to obtain the stress-strain responses under MCs, it is assumed that the applied load is purely axial and no volume changes during deformation (Dehm et al., 2018; Greer et al., 2005). Then, the engineering stress can be calculated by F/A, where F is the measured force and A is the cross-sectional area at 20 % height of the as-prepared pillar considering that the deformation is concentrated near the pillar top region due to the taper (Guo et al., 2014; Li et al., 2020; Wu et al., 2024). The engineering strain was calculated by x_c/L, in which the L is the original pillar height and x_c is the corrected displacement which can be written as (Frick et al., 2008):

$$x_c = x - \frac{(1 - \nu_r^2)F}{E_r d_t} - \frac{(1 - \nu_{si}^2)F}{E_{si} d_b} \tag{1}$$

where x is the measured displacement. d_t and d_b are the diameters of the pillar top and bottom, respectively. E_r and ν_r denote the Young's modulus and Poisson's ratio of the diamond indenter and are taken to be 1220 GPa (Spear and Dismukes, 1994) and 0.2 (Gan et al., 1996) respectively. E_{si} and ν_{si} represent the Young's modulus and Poisson's ratio of the Si substrate, which are 130 GPa (Hopcroft et al., 2010) and 0.278 (Gan et al., 1996), respectively. Besides, in order to obtain the peak stress and strain hardening rate of each sample, the true stress and true strain were converted from the engineering stress-strain data based on the conventional assumption that the pillars deform homogeneously with unchanged volume during deformation, i.e., $\sigma_t = \sigma_e(1 + \varepsilon_e)$ and $\varepsilon_t = \ln(1 + \varepsilon_e)$, where σ_t, σ_e, ε_t and ε_e represent the true stress, engineering stress, true strain and engineering strain, respectively.

2.3. Microstructural characterization

The microstructures of the as-prepared Nb/amorphous CuNb NMFs were characterized by TEM and scanning TEM (STEM). The TEM lamellas were prepared by FIB (FEI Helios 5CX). The final milling voltage and the current were 5 kV and 18 pA, respectively, which was small enough to reduce the FIB damage. The bright-field TEM graphs, high-angle annular dark field (HAADF)-STEM images, and energy dispersion spectrum (EDS) mapping were taken by a Talos F200X G2 operated at 200 kV. The selected area electron diffraction (SAED) and the high-resolution TEM (HRTEM) micrographs were performed in a spherical aberration-corrected TEM (FEI Titan Themis G2 60-300) operated at 300 kV. The morphologies of the micropillars before and after deformation were examined in a scanning electron microscopy (SEM) (FEI Helios 5CX) at a 52°-tilted angle to clearly show the pillar morphology because the as-prepared pillar was fabricated to be vertical to the substrate. The used voltage/current was 5 kV/80 pA. The morphology of the micro-indents was taken in a field-emission SEM (Tescan Mira 3) using a voltage of 20 kV. Furthermore, the cross-sectional TEM lamellas of the deformed pillars were prepared by FIB and characterized by TEM, in order to investigate the microstructure evolution of the pillar after compression.

3. Results and discussion

3.1. Microstructures of the Nb/amorphous CuNb NMFs

The cross-sectional bright-field TEM image (Fig. 2a) shows the as-prepared NMF ($h = 40$ nm) with a well-defined alternating of Nb layer and amorphous CuNb layer. The Nb layers in the composite present a polycrystalline structure and grow with a strong (110) texture, as revealed by the SAED pattern (inset in Fig. 2a). The HRTEM image in Fig. 2b provides an atomic-level observation of the crystalline-amorphous interface (indicated by the dashed line), beside which the amorphous structure with disorder atoms and the BCC crystalline with ordered atomic arrangement can be well identified. The fast Fourier transformation (FFT) patterns (insets in Fig. 2b) further reveal the amorphous halo ring of the amorphous CuNb layer and typical BCC crystal orientations of the Nb layer observed along the [111] zone axis. The detected actual composition of the amorphous layer is $Cu_{62.3}Nb_{37.7}$, which is close to the designed value, i.e., $Cu_{60}Nb_{40}$. In addition, the composition of the amorphous layer is almost homogeneously distributed along the thickness direction, as seen from the probed EDS mapping (Fig. 2d) and the corresponding line scanning profile (Fig. 2e). There appears a gradient in the composition near the Nb–CuNb interface regions, i.e., the transition region from one layer to the another (indicated by gray shadows in Fig. 2e), which is owing to the limited resolution of EDS. This is the common instrumental limitation at such small scale (several nanometers space of the interface region) for STEM-EDS and even atom probe tomography (Wu et al., 2021). Note that there exists significant Cu content in the Nb layers due to that the used holder for the TEM specimen was copper grid and the mixing of more mobile Cu during the FIB preparation of the TEM specimen. Additionally, the 100 nm and 5 nm samples share a similar microstructure with the 40 nm one (e.g., columnar grains, strong (110) texture, distinct crystalline-amorphous interface), as presented in more detail in the previous work of the authors (Qin et al., 2024).

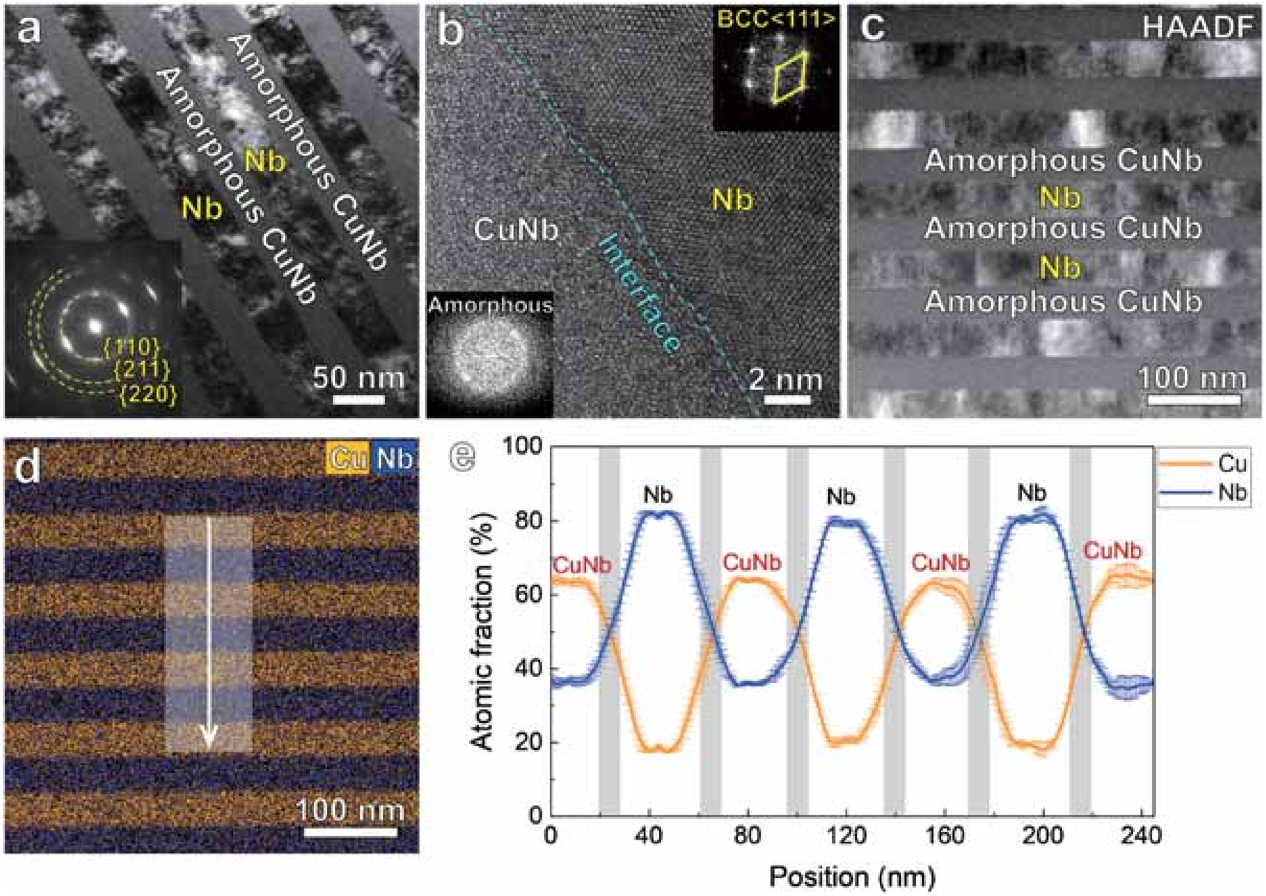

Fig. 2. Microstructures of the Nb/amorphous CuNb film. (a) Typical cross-sectional bright-field TEM image of the film with a layer thickness of 40 nm, where the inset is the corresponding SAED pattern. (b) HRTEM micrograph of the crystalline-amorphous interface region. The insets in (b) are the FFT patterns of crystalline Nb and amorphous CuNb layers, respectively. (c) HAADF-STEM image. (d) The corresponding EDS mapping. (e) EDS line scanning profile along the arrow indicated in (d), revealing the chemical composition in the thickness direction. The gray shadows in (e) designate the Nb-CuNb interfacial regions. The error bars of the curves in (e) indicate statistical errors in terms of the standard deviations.

3.2. Mechanical response of single-phase amorphous CuNb and polycrystalline Nb monolayer films under MCs

Fig. 3 shows the deformed pillars of the single-phase amorphous CuNb monolayer film under different applied strains. The pillar exhibits elastic deformation followed by a jerky-type deformation with shear banding events, which correspond to strain bursts in the engineering stress-strain curves (Figs. 3a-l). In Fig. 3a, two SBs initiated sequentially from the pillar top (marked by red arrows), which is probably due to the combined effect of the pillar taper and the initial imperfect pillar-punch contact (Chen et al., 2010), causing the sequential appearance of bursts at 3.5 % and 5 % strains (Fig. 3d). With higher straining, the pillar deforms with the catastrophic major shear banding process. This process is associated with the generation and propagation of multiple SBs (Figs. 3b-i), i.e. the primary SBs (marked by red arrows in Figs. 3b and c) and a few neighboring secondary SBs (marked by blue arrows in Figs. 3b and c), causing the serrations type in the stress–strain curves (e.g., see Figs. 3e and f). Interestingly, the occurrence of multiple SBs does not seem to weaken the pillar. This may be attributed to the increase of the load-bearing diameter with these multiple SBs (Figs. 3b-h), enabling the pillar to bear a higher load upon further loading. The amorphous pillar is not completely fractured even after the major shear banding process with straining up to 59.1 % (Fig. 3i), which can be explained by an extrinsic size effect (Greer and De Hosson, 2011), since the critical shear offset size (~10–20 μm) at which catastrophic failure that happens in bulk MGs (Conner et al., 2003; Ravichandran and Molinari, 2005) cannot be reached in such small pillar.

In contrast to the amorphous sample, the single-phase polycrystalline Nb monolayer film shows stable plastic deformation and obviously continuous strain-hardening, as revealed by the SEM images and stress–strain curves (Fig. 4). The Nb pillar shows a slight

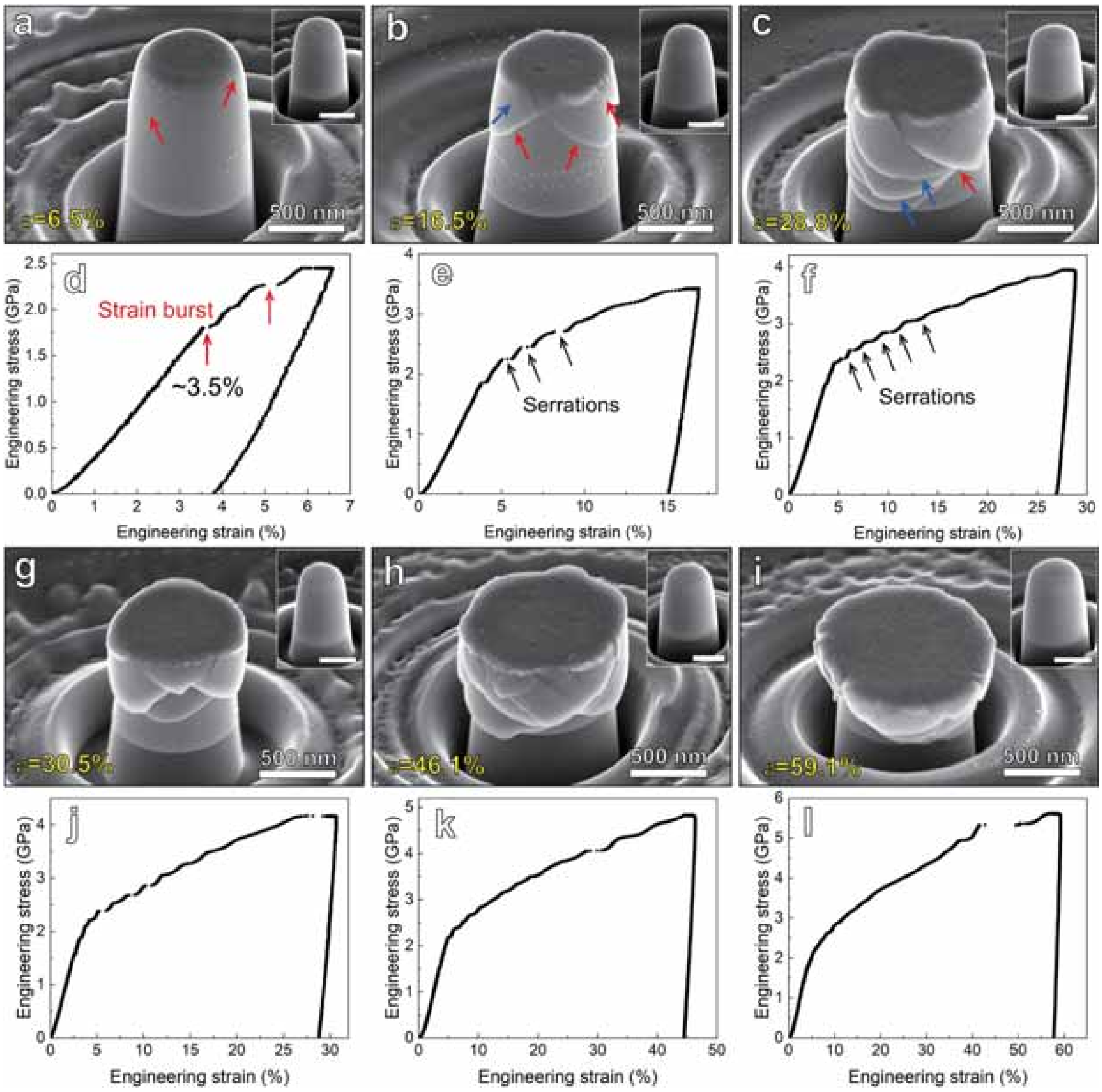

Fig. 3. Mechanical response of the single-phase amorphous $Cu_{60}Nb_{40}$ monolayer film under MCs subjected to different applied strains (from 6.5 % to 59.1 %). (a-c, g-i) 52°-tilted SEM images of the deformed pillar, where the insets are the as-prepared pillars. (d-f, j-l) Corresponding engineering stress–strain curves. Scale bars in the insets: 500 nm.

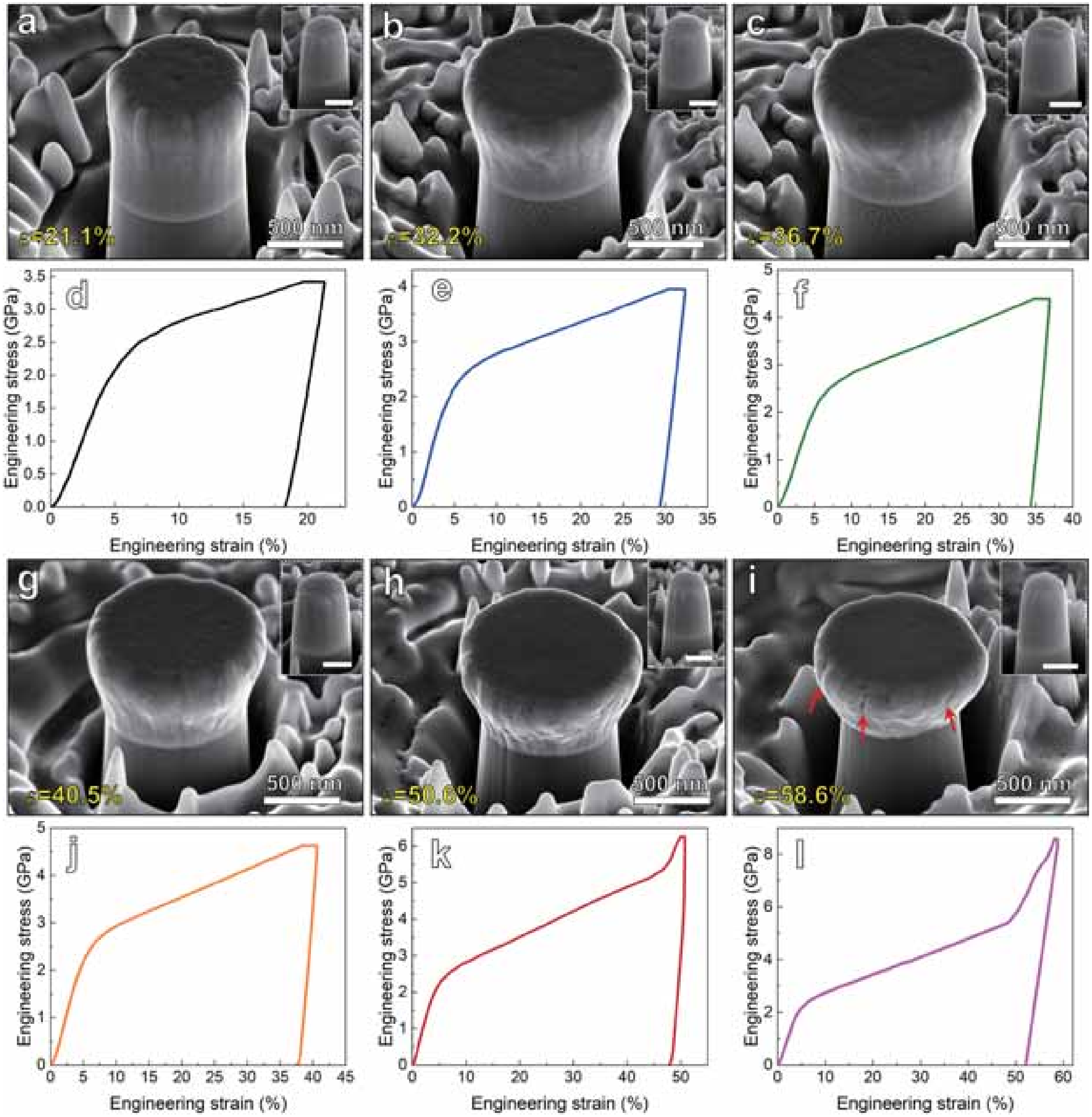

Fig. 4. Mechanical response of the monolayer Nb film under MCs subjected to different applied strains (from 21.1 % to 58.6 %). (a-c, g-i) 52°-tilted SEM images of the deformed pillar, where the insets are the as-prepared pillars. (d-f, j-l) Corresponding engineering stress–strain curves. Scale bars in the insets: 500 nm.

barreling deformation near the pillar top at a small applied strain (21.1 %, Fig. 4a). The pillar deforms with a mushroom-like with higher straining processes (Figs. 4b-h), which is a typical deformation behavior of columnar-grained nanostructured metals, as similarly observed in NbMoTaW nanopillars (Zou et al., 2015). At higher applied strain (58.6 %), the pillar experiences cracking at the pillar top parts, and cracks propagate along grain boundaries (indicated by red arrows in Fig. 4i), showing intergranular fracture behavior. Note that a sudden stress increase occurs at ~45 % strain (Figs. 4k and l), which was presumedly induced by the combined effect of the bulking-induced strong hardening and the mechanical response of the Si substrate.

3.3. Mechanical response of the Nb/amorphous CuNb NMFs under MCs

3.3.1. Stress–strain responses of the Nb/CuNb NMFs

Fig. 5 presents the engineering stress–strain curves of the Nb/CuNb NMFs with layer thickness 100 nm, 40 nm and 5 nm under MCs, in which small and large pillars are incorporated. The results show that obvious elastic deformation followed by a stable plastic flow can be observed from these curves in the 100 nm (Figs. 5a and d) and 40 nm (Figs. 5b and c) samples for both the small and large pillars. In the 5 nm sample, however, a stress drop occurs at an applied strain of 43 % for small pillars (e.g., $D = 594$ nm, see Fig. 5e) and at and applied strain of 42 % for large pillars (e.g., $D = 725$ nm, see Fig. 5f), which suggests the onset of compression instability, e.g., shear banding. The continuous stress increases after this stress drop may be attributed that the stress drop induced by the shear banding is

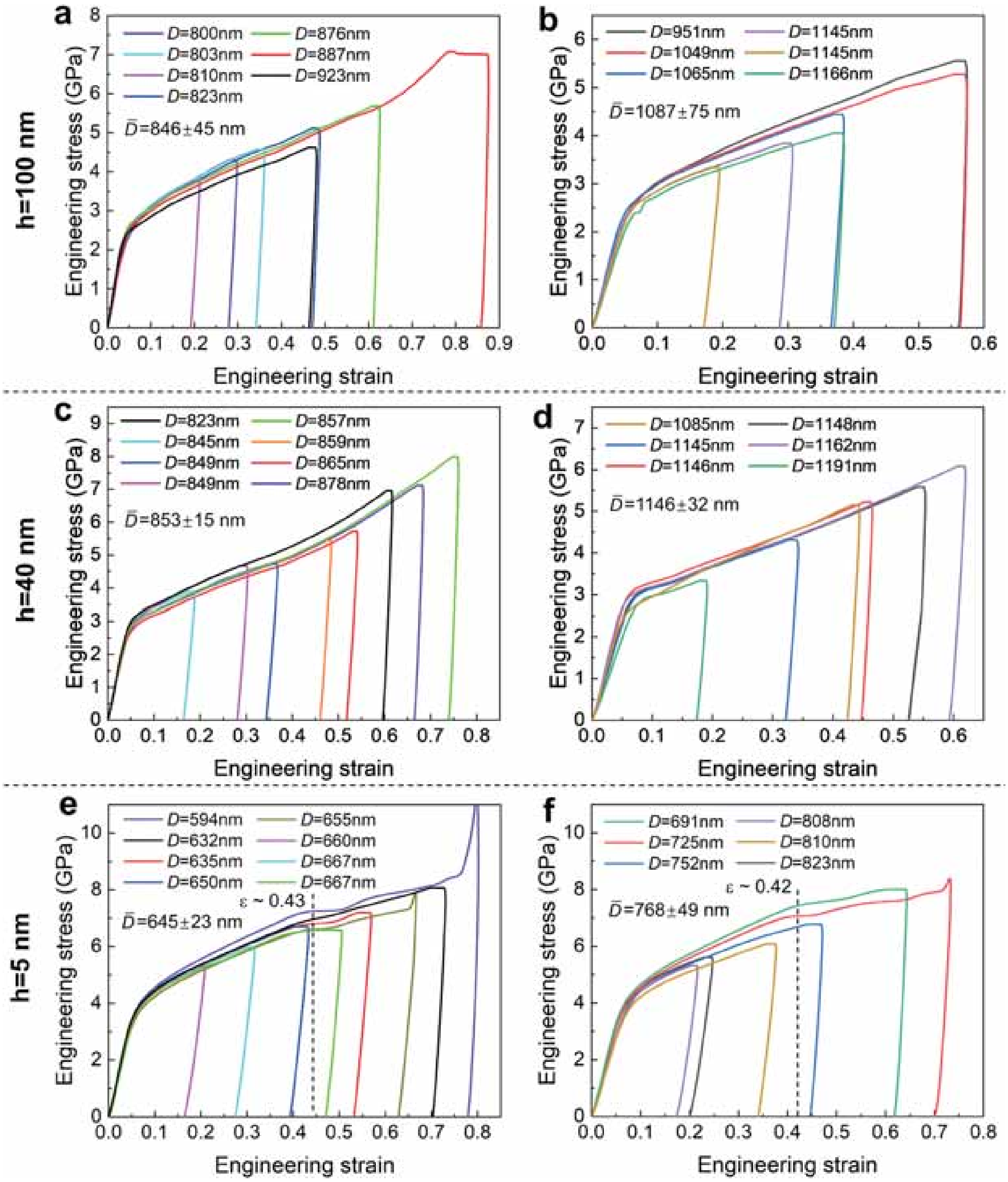

Fig. 5. Engineering stress–strain curves of the (a, c, e) small and (b, d, f) large pillars in the Nb/amorphous CuNb NMFs with layer thickness of (a, b) 100 nm, (c, d) 40 nm, and (e, f) 5 nm under MCs. The black dashed line in (e, f) indicates the applied strain at which the stress drop occurs in the 5 nm sample.

compensated by the stress caused by the increase of pillar diameter with the deformation process. Note that there appear some discrepancies in the stress-strain curves for each sample with small (Figs. 5a, c, e) or large (Figs. 5b, d, f) pillar diameters, presumably owing to the discrepancies in the diameter of each specific as-prepared pillar, because the strength of materials usually increases with decreasing diameter (Cao et al., 2019; Greer et al., 2005; Uchic et al., 2004; Volkert and Lilleodden, 2006; Zhang et al., 2012b).

Besides, for the three samples, the deviation from linearity in the engineering stress-strain curves is observed earlier in the large pillars than in the small ones (see Supplementary Fig. 1). This may be attributed to a larger taper in large pillars than in these small pillars since the stress concentration at the pillar top may lead to easier yielding due to the tapered sample geometry (Uchic et al., 2009). Therefore, in order to estimate the yield strength more accurately, the flow stress at 2 % and 3 % plastic strain was adopted as the yield strength for the three samples with small pillars and large pillars, respectively, as illustrated in Supplementary Fig. 1. In addition, the peak stress in the true stress-strain curves (Supplementary Fig. 2.) is determined as the ultimate strength of the Nb/CuNb

NFMs.

3.3.2. Extrinsic and intrinsic size-dependent strength of the Nb/CuNb NMFs

The pillar diameter and layer thickness-dependent yield strength and ultimate strength of the Nb/CuNb NFMs are summarized in Fig. 6. First, it can be found that both the yield strength and the ultimate strength of the Nb/CuNb NMFs are increased with the decrease of pillar diameter (Figs. 6a and b), which is a typical extrinsic size effect as observed in existing MCs (Greer et al., 2005; Uchic et al., 2004; Zhang et al., 2012b). The pillar diameter effect can be described by a power law (Uchic et al., 2009), i.e., $\sigma = CD^{-n}$, where C is a constant, and n is the power-law exponent. It can be found that the values of n are decreased with the reduction of layer thickness (Figs. 6a and b), indicating that the extrinsic size-induced strengthening is weakened with decreasing layer thickness. This can be explained by that the crystalline phase-dominated plastic flow of the Nb/CuNb NMFs is gradually transited to the amorphous phase-denominated one with the decrease of layer thickness, while amorphous metals generally show size-independent strength (Chen et al., 2010).

Second, the yield strength of the Nb/CuNb NMFs first increases with the decreasing layer thickness h and then reaches a plateau at $h = 5$ nm (Fig. 6c). This phenomenon is different from the softening usually observed in crystalline/crystalline (e.g., Mg/Nb (Ham and Zhang, 2011), Cu/Nb (Misra et al., 2005)) NMFs when h is below 5 nm, which demonstrates the enhanced strengthening capability of the BCC crystalline-amorphous interface. The intrinsic size (layer thickness)-dependent strengthening of the Nb/CuNb NMFs with layer thickness ranging from 100 nm to 10 nm can be well described by the confined layer slip (CLS) theory (Misra et al., 2005), as demonstrated in our previous study (Qin et al., 2024). The layer thickness-independent strength at $h < 10$ nm was attributed to the amorphous phase-dominated plastic flow in the Nb/CuNb NMFs at such small scale (Qin et al., 2024). Besides, the yield strength of the Nb/CuNb NMFs determined by MC shows a good agreement with the nano-hardness ($H/2.7$). It has been reported that the true stress at 8 % strain ($\sigma_{8\,\%}$) shows a good agreement with $H/2.7$ for NMFs, e.g., Cu/Nb (Mara et al., 2010). However, the $H/2.7$ underestimates

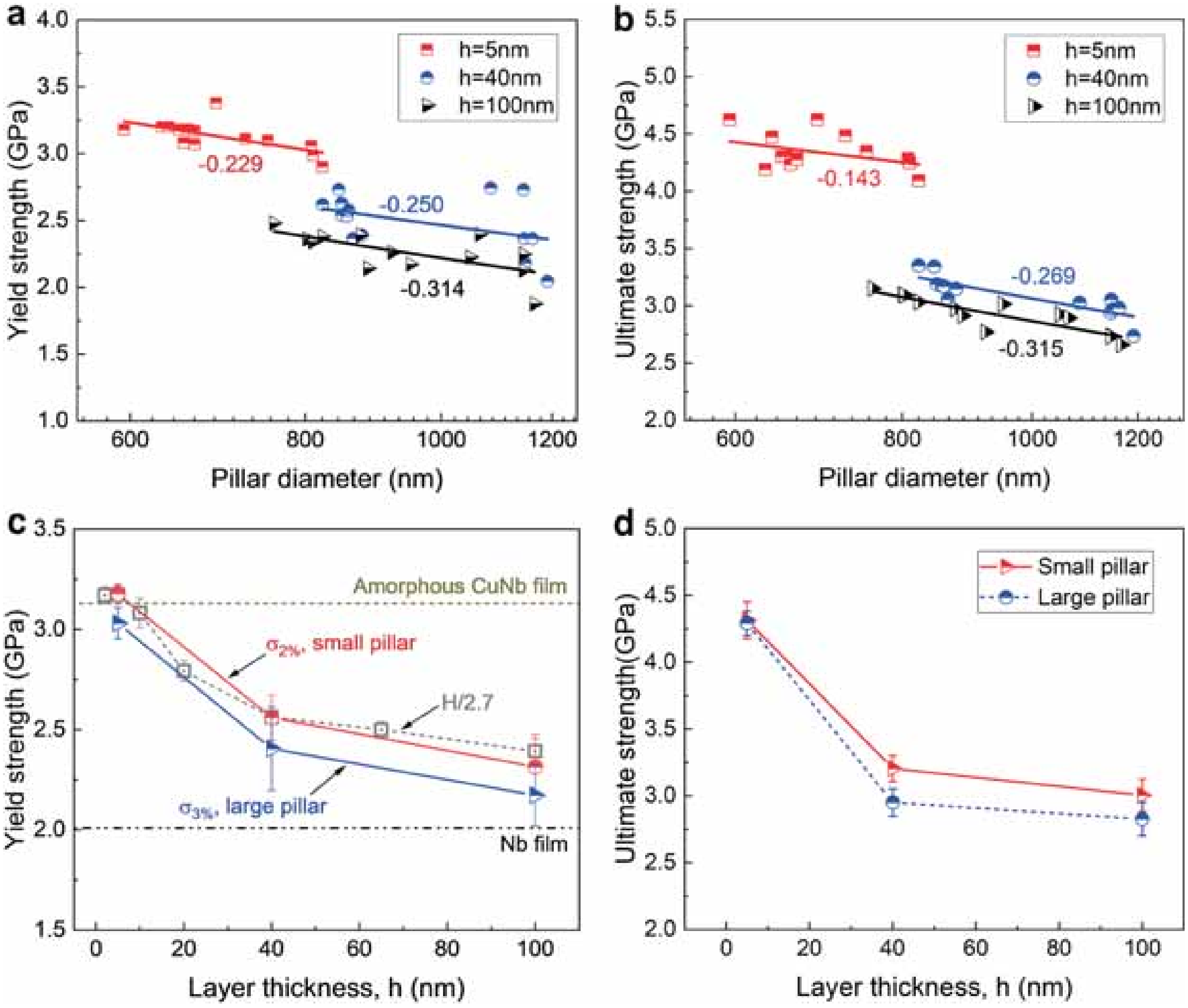

Fig. 6. The (a, b) pillar diameter and (c, d) layer thickness dependent yield strength and ultimate strength of the Nb/amorphous CuNb NMFs. The average diameters of the small pillars are 846 ± 45 nm for the 100 nm sample, 853 ± 15 nm for the 40 nm sample, and 645 ± 23 nm for the 5 nm one. The corresponding values for the large pillars for the three samples are 1087 ± 75 nm, 1146 ± 32 nm and 768 ± 50 nm, respectively. In (c), the data of the yield strength is evaluated as the nano-hardness (H) divided by 2.7, which were adopted from Qin et al. (2024). The corresponding data of the monolithic Nb and amorphous CuNb thin films are also included for comparison.

$\sigma_{8\,\%}$ for the Nb/CuNb NMFs (see Supplementary Fig. 4). This may be attributed to that the Nb/CuNb NMF has a large mismatch ($\sigma_{\mathrm{CuNb}}/\sigma_{\mathrm{Nb}} > 1.5$) in constituent flow strength (Gram et al., 2015). In addition, due to the difference in pillar diameters, the strength of the Nb/CuNb NMFs with large pillars and small pillars shows a slight discrepancy (less than 0.3 GPa), as shown in Figs. 6c and d. Specifically, the yield strength is decreased from 2.31 GPa to 2.17 GPa for the 100 nm sample (with pillar diameter increasing from 846 nm to 1087 nm), from 2.56 GPa to 2.40 GPa for the 40 nm sample (with pillar diameter increasing from 853 nm to 1146 nm), and from 3.18 GPa to 3.03 GPa for the 5 nm sample (with pillar diameter increasing from 645 nm to 768 nm). The corresponding ultimate strength (Fig. 6d) is decreased from 3.01 GPa to 2.83 GPa for the 100 nm sample, from 3.20 GPa to 2.95 GPa for the 40 nm sample, and from 4.32 GPa to 4.29 GPa for the 5 nm one.

3.3.3. Comparison between the mechanical behaviors of the Nb/CuNb NMFs and their constituent phases

To clearly exhibit the stress–strain response and the strain-hardening behavior of all samples, only one typical true curve for each sample was selected to be presented in Fig. 7a because all the curves of different pillars with similar diameters for the same sample are very close to each other (see Supplementary Fig. 2). Typical serrations are observed in the curve of the amorphous $Cu_{60}Nb_{40}$ film, which usually indicates the propagation of multiple SBs, similar as observed in the deformed pillars of the amorphous $Cu_{50}Nb_{50}$ film (Fan et al., 2017b) and other MGs (Chen et al., 2010; Greer and De Hosson, 2011). However, there are no serrations in the stress–strain curves of the monolithic Nb film and the three NMFs. Instead, significant strain hardening has been stimulated, indicating that the shear banding is suppressed. Note that the strain hardening rate ($d\sigma_t/d\varepsilon_t$) of the 5 nm sample is lower than that of the 40 nm and 100 nm samples (Fig. 7b), which is owing to the limited dislocation accumulations and interactions within such small layer thickness (Meyers et al., 2006).

Besides, note that the flow stress of the 5 nm sample is even higher than that of the amorphous CuNb sample (Fig. 7a), which might be attributed to the coupling of the intrinsic (layer thickness) and extrinsic size (pillar diameter) strengthening effect because the strength of the NMFs is increased with decreasing layer thickness and pillar diameter. This phenomenon is common in crystalline-amorphous NMFs under MC. For example, Zhang et al. (2012c) reported that the amorphous CuZr sample shows a size-independent ultimate strength of 1850 ± 350 MPa even the pillar diameter ranges from 100 nm to 1000 nm. However, the 5 nm Cu/amorphous CuZr sample with a pillar diameter of 350 nm reaches an ultimate strength of 4.8 GPa, which is about 2.4 times that of the hard amorphous phase. The above finding demonstrates that the Nb/CuNb NMFs achieve a better strength-plasticity balance than their constituent phases.

3.3.4. MC-induced deformation evolution in the Nb/CuNb NMFs

A series of pillars with small and large diameters for all the three samples were prepared in order to investigate the extrinsic (pillar diameter) and intrinsic (layer thickness) size dependence of the mechanical response of the Nb/CuNb NMFs under MCs. Fig. 8 shows the deformation evolution of the small pillars in the Nb/CuNb NMFs under MCs. Three different types of deformation morphologies can be observed in the samples with h of 100 nm (Figs. 8a_1–a_6), 40 nm (Figs. 8b_1–b_6) and 5 nm (Fig. 8c_1–c_6). For the 100 nm sample, the deformation transmits from a homogeneous-like (Fig. 8a_1) to profuse localized extrusions (Fig. 8a_3) as the applied strain increases from 21.2 % to 36.1 %. This inhomogeneous extrusion becomes more and more severe with the deformation processing (Fig. 8a_4), which is distinct from the extrusion in homogenous and ring-type as observed in crystalline/crystalline NMFs (Li et al., 2020, 2017). Furthermore, micro-cracks occur in the deformed pillar at a strain of 64.8 % (Fig. 8a_5), and the pillar subsequently fails via a full fracture at 87.6 % strain (Fig. 8a_6). The 40 nm sample exhibits a homogeneous deformation with the plastic barreling extending from the pillar top to the bottom even with compressed straining to 48.5 % (Figs. 8b_1–b_4). Some micro-cracks occur in the pillar at 64.8 % strain (Fig. 8b_5). Intriguingly, the pillar is flattened homogeneously without fracturing even under a large strain of 76.1 % (Fig. 8b_6),

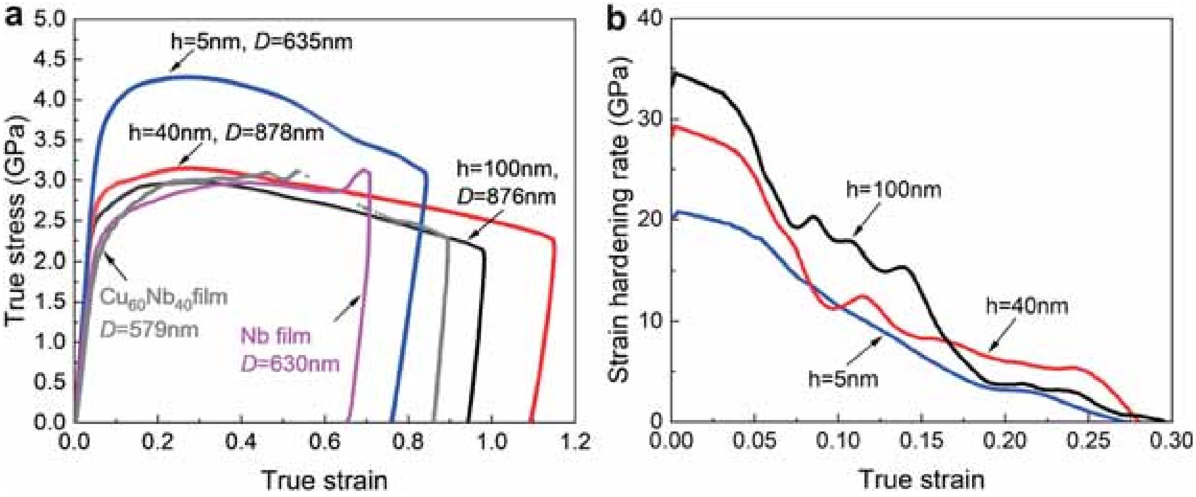

Fig. 7. Mechanical responses of the Nb/amorphous CuNb NMFs with layer thickness of 5 nm, 40 nm and 100 nm, in comparison with the monolithic Nb and amorphous CuNb thin films under MCs. (a) Representative true stress–strain curves. (b) The variation of strain hardening rate with respect to the applied strain.

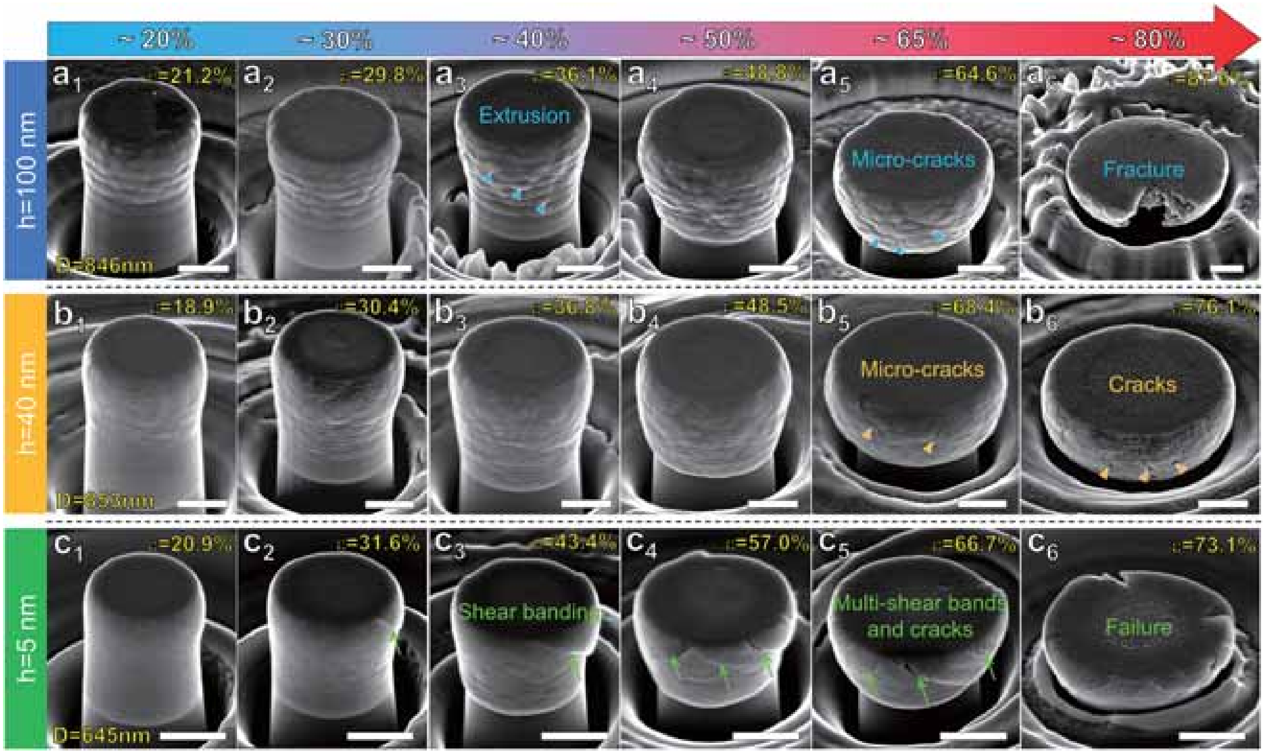

Fig. 8. The evolution of the MC-induced deformation of the small pillars in the Nb/amorphous CuNb NMFs with different layer thickness (a_1–a_5) $h = 100$ nm, $D = 846$ nm, (b_1–b_5) $h = 40$ nm, $D = 853$ nm, (c_1–c_5) $h = 5$ nm, $D = 645$ nm. Scale bars: 500 nm.

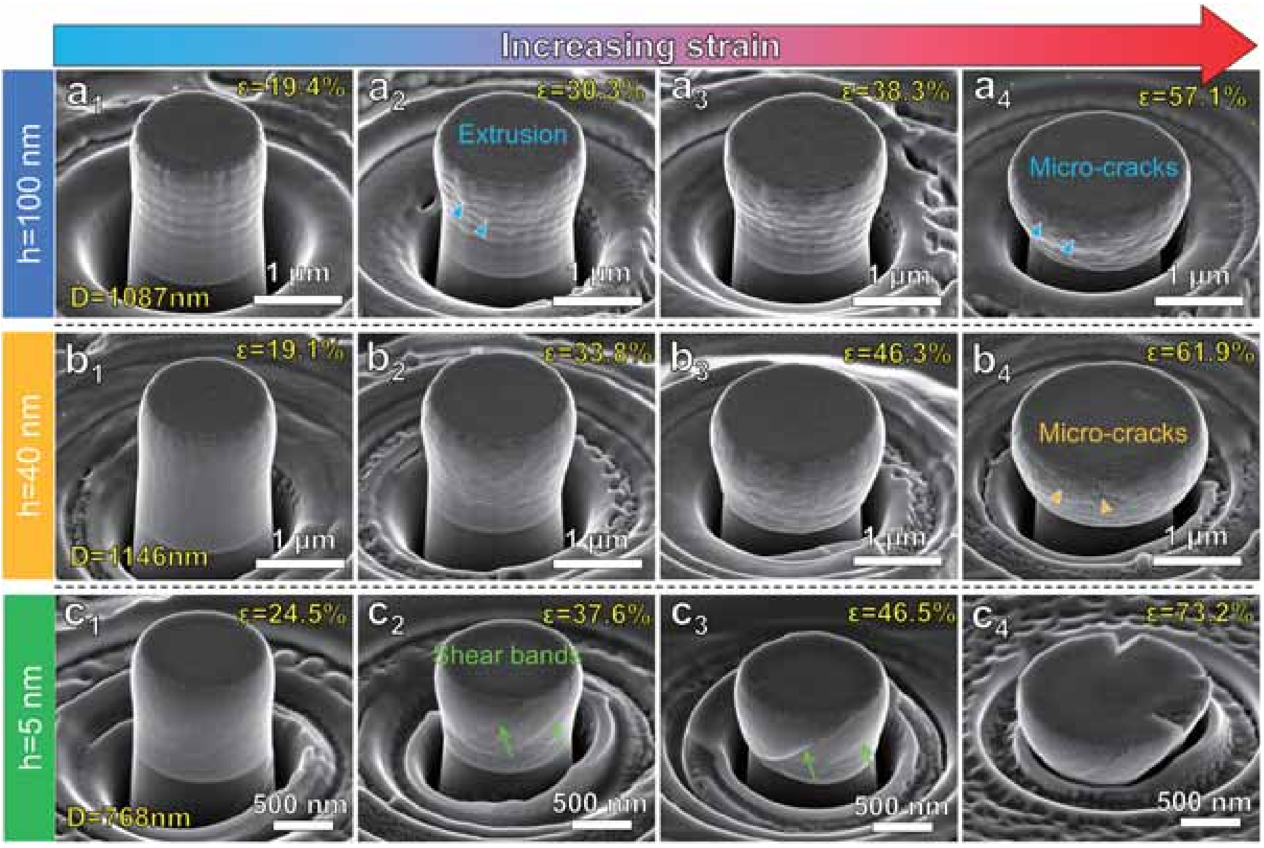

Fig. 9. The evolution of the MC-induced deformation of the large pillars in the Nb/amorphous CuNb NMFs with different layer thickness, (a_1–a_5) $h = 100$ nm, $D = 1087$ nm, (b_1–b_5) $h = 40$ nm, $D = 1146$ nm, (c_1–c_5) $h = 5$ nm, $D = 768$ nm.

which suggests the exceptional deformability of the 40 nm sample. For the 5 nm sample, the pillar shows a homogeneous deformation at a relatively small strain of 20.9 % (Fig. 8c_1). However, a slight shear step occurs near the pillar top as the strain increases to 31.6 % (Fig. 8c_2), which suggests the onset of the shear banding. The SB initiated from the pillar top throughout the pillar at 43.4 % strain (Fig. 8c_3). Moreover, profuse SBs and cracks are formed in the pillar at higher strain (Figs. 8c_4 and c_5). A complete failure with a number of cracks and SBs occurs after a 73.1 % compression strain (Fig. 8c_6). It is worth noting that both the 100 nm and 5 nm samples can be deformed to bear an applied strain of 50 % without macro-failure, but this does not essentially reflect their true compressive fracture elongation. These rather large apparent compressive strain values may be partially caused by the inhomogeneous plastic flow induced by shear/slip band percolation during pillar deformation, e.g., the inhomogeneous extrusion in the deformed pillars of the 100 nm sample (Figs. 8a_2-a_4) and multiple SBs in those of the 5 nm ones (Figs. 8c_4-c_5), instead of catastrophic fracture (Dehm et al., 2018; Wu et al., 2020).

Fig. 9 presents the mechanical response of the large pillars for all the three samples, i.e., $D = 1087$ nm for the 100 sample, 1146 nm for the 40 sample 768 nm for the 5 nm one. The results show that for the 100 nm sample, the pillar deforms homogeneously with a barreling shape under a 19.4 % applied strain (Fig. 9a_1). Significant extrusion deformation occurs in the deformed pillars (indicated by blue triangles in Fig. 9a_2) under higher applied strains, e.g., 30.3 % (Fig. 9a_2) and 38.3 % (Fig. 9a_3). Micro-cracks were observed in the pillar after being subjected to an applied strain of 57.1 % (Fig. 9a_4). For the 40 nm sample, the pillars exhibit homogenous deformation as the applied strain is increased from 19.1 % to 46.3 % (Figs. 9b_1-b_3), which demonstrates its excellent compressive plasticity. Following the homogeneous deformation, micro-cracks are detected in the pillar under an applied strain of 61.9 %. As for the 5 nm sample, the pillar shows a homogenous deformation at an applied strain of 24.5 % (Fig. 9c_1). With the applied strain proceeding, the pillar undergoes severe shear banding in the form of the propagation of multiple SBs (Figs. 9c_2-c_3). At a higher applied strain (73.2 %), the pillar shows a complete failure associated with localized SBs and cracks (Fig. 9c_4). The above finding shows that the observed deformation of the large pillar is qualitatively consistent with the small ones (Fig. 8).

The above MC results indicate that the extrinsic size effect on the strength (Fig. 6) and plasticity (Figs. 8 and 9) of the Nb/CuNb NFMs is not insignificant. This insignificant change might come from that the in-plane grain size is much smaller than the pillar diameters for the present Nb/CuNb NMFs, i.e., the in-plane grain size is 76.8 ± 2.5 nm for $h = 100$ nm, 50.4 ± 0.7 nm for $h = 40$ nm and 11.3 ± 0.3 nm for $h = 5$ nm, as measured from the cross-sectional TEM micrographs of the as-prepared films in our previous study (Qin et al., 2024). Note that the pillar diameter is at least 800 nm for $h = 100$ nm; 845 nm for $h = 40$ nm and 593 nm for $h = 5$ nm, which is

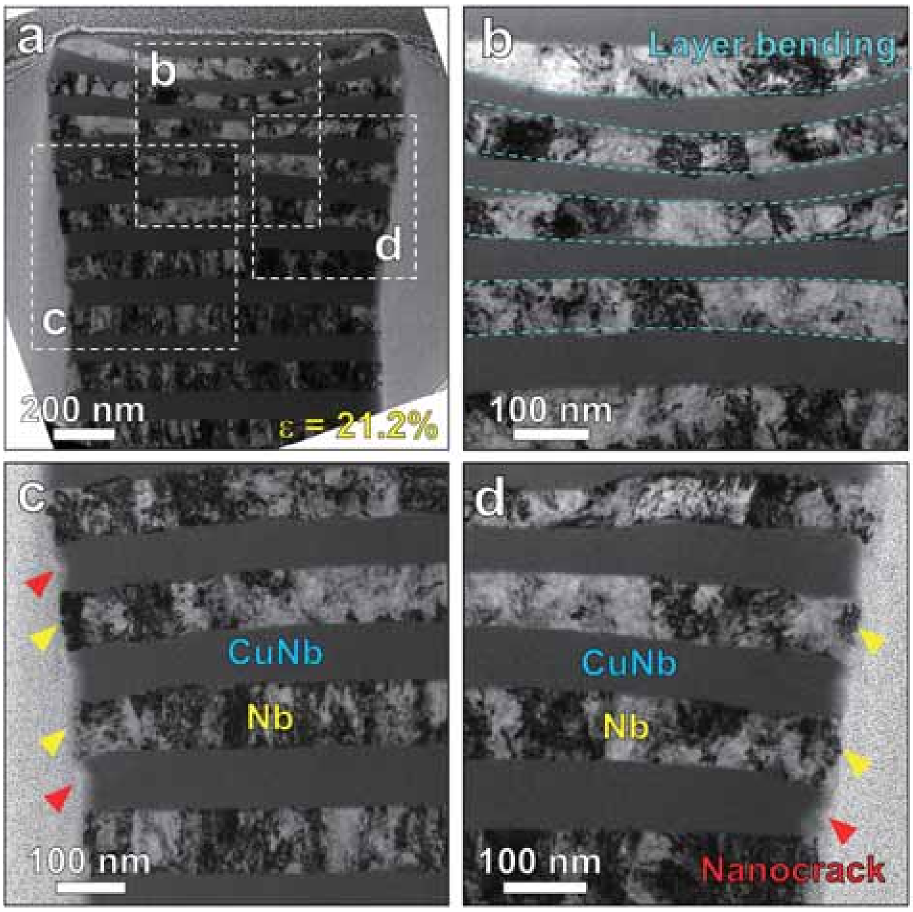

Fig. 10. Cross-sectional microstructures of the deformed pillar ($D = 810$ nm) under an applied strain of 21.2 % for the 100 nm sample. (a) Bright-field TEM image. (b) High-magnification TEM images of the localized deformation region near the pillar top. (c) and (d) are the enlarged TEM images of the left and right sides of the deformed pillar, respectively.

10 times larger than the grain size of the Nb layer. Usually, the mechanical size effect appears when the sample size becomes comparable to the correlation length of the defects that carry the plastic deformation (Uchic et al., 2004), that is, extremely small samples with low probability of containing defects or defect sources are usually stronger than those contain a mean field equivalent defect population (Wu et al., 2020).

3.3.5. *Microstructure evolution and deformation mechanism of the Nb/CuNb NMFs under MCs*

To reveal the MC-induced microstructure evolution and deformation mechanism of the Nb/CuNb NMFs, the deformed pillars under different applied strains for the three samples were investigated by TEM. For the 100 nm sample, the deformed pillar under an applied strain of 21.2 % shows a typical barreling shape with plastic deformation concentrating near the pillar top (Fig. 10a). The layers at the pillar top show obvious bending (Fig. 10b). From the high magnification TEM image (Figs. 10c and d), it can be found that the crystalline Nb layers are slightly squeezed out (indicated by the yellow triangles) due to the lower yield strength of the Nb layer than that of the amorphous one, which is similar to the deformation feature observed in Cu/Zr pillars (Zhang et al., 2012b) and Cu/amorphous CuZr pillars (Zhang et al., 2012c) under MC. In addition, embryo nano-cracks are observed in the amorphous CuNb layers, as indicated by the red triangles. However, no mature cracks form. The MC-measured plasticity of the Nb/CuNb NMFs is adopted as the maximum applied strain without forming micro/nano-cracks and shear banding in the deformed pillars, which is called as the MC-measured homogeneous deformation strain (HDS, $\varepsilon_{\mathrm{HDS}}^{\mathrm{MC}}$), as similarly used by other researchers, e.g., (Chen et al., 2020c; Cheng et al., 2022; Wu et al., 2020, 2023a). Thus, the above applied strain of 21.2 % can be approximated as the HDS, i.e., $\varepsilon_{\mathrm{HDS}}^{\mathrm{MC}} = 21.2\,\%$, for the 100 nm sample.

At higher applied strain (36.1 %), the deformed pillar exhibits a more obvious barreling shape (Fig. 11a). The Nb layers near the pillar top show an inhomogeneous thinning (Fig. 11b). For instance, the layer is even deformed to 23 nm near the pillar center whereas the region away from the pillar center can reach 50 nm, which corresponds to a strain difference of 27 % by dividing the initial layer thickness (100 nm). This inhomogeneous thinning of the Nb layers may be attributed to the non-symmetric slip activity of dislocations induced by the bending/rotation of the constituent layers (Mara et al., 2010). A few dislocation pileups are detected in the Nb layer near the top region of the deformed pillar, as indicated by the green triangles in Fig. 11b.

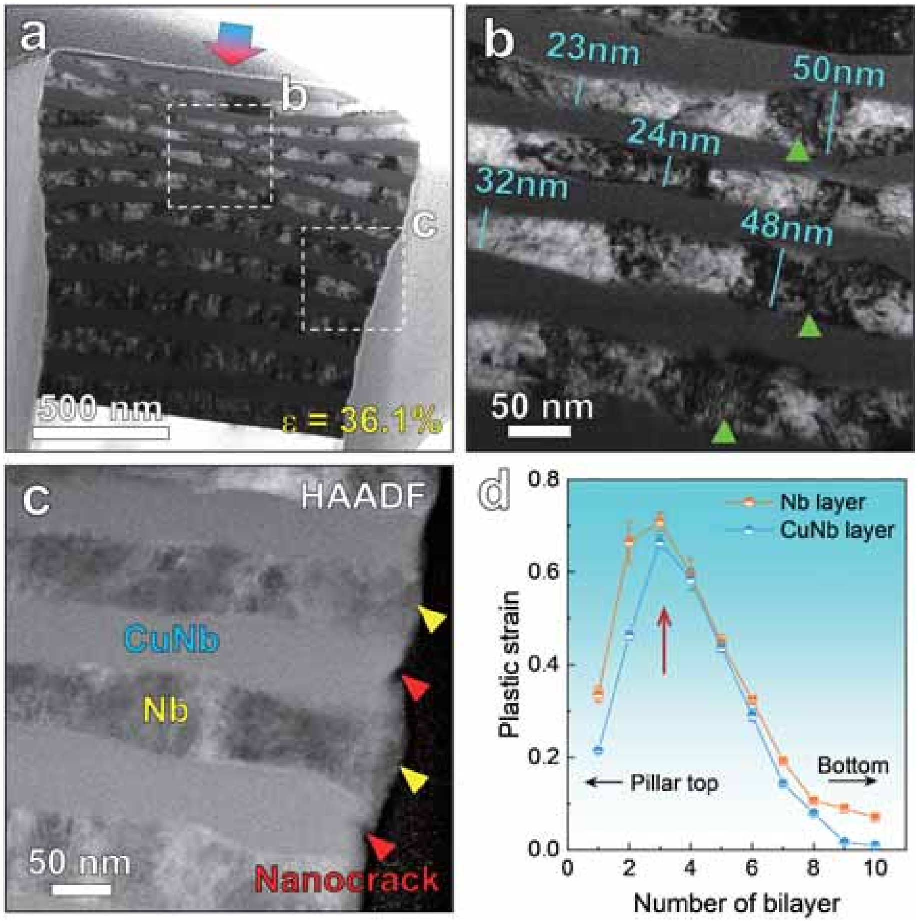

Fig. 11. Cross-sectional TEM microstructures of the deformed pillar (D = 803 nm) under an applied strain of 36.1 % for the 100 nm sample. (a) Bright-field TEM image. (b) A high-magnification observation of the severely deformed region. (c) HAADF-STEM image of the pillar side. (d) The distribution of the plastic strains of the Nb and amorphous CuNb layers from the pillar bottom to the top along the pillar axis, as calculated from the measurements of the change of the layer thickness before and after deformation from (a).

In nanocrystalline materials, grain boundaries generally serve as dislocation sources and sinks (Bitzek et al., 2008; Schiøtz and Jacobsen, 2003; Van Swygenhoven et al., 2006). Continued plastic deformation is contingent on a succession of quantized events that percolate throughout the polycrystal (Li et al., 2009). In contrast, NMFs have specific heterogeneous interfaces, e.g., typical {111} Cu//{110}Nb Kurdjumov-Sachs (K-S) interface observed in Cu/Nb NMFs prepared by rolling (Anderson et al., 2003) and magnetron sputtering (Chen et al., 2020c). Thus, dislocation nucleation events start priority in layered interfaces rather than the grain boundaries in NMFs (Li et al., 2012; Wang et al., 2007). Therefore, the dislocation would first emit from the crystalline-amorphous interface near regions of the high atomic slip in the amorphous phase (Cheng and Trelewicz, 2016). Part of the dislocations within the Nb layer reaching the crystalline-amorphous interface will be absorbed by the interface (Cheng and Trelewicz, 2016; Wang et al., 2024, 2007), while a few dislocations may accumulate within the grains. In particular, slip occurs in the closest packed ⟨111⟩ direction and the Burgers vector is a/2 ⟨111⟩ for BCC metals (Weinberger et al., 2013). There is an increasing propensity for diffuse, wavy slip, and slip activity observed on {110}, {112} and {123} planes at room temperature or high temperature (Lee et al., 2023; Lim et al., 2020; Weinberger et al., 2013; Wen et al., 2023). Thus, the dislocation pile-up may occur in several slip planes of the Nb layer, e.g., {110} and {112} planes. Moreover, it can be noted that there are high-density dark spots and dark linear shapes distributed homogeneously in these Nb layers near the pillar bottom (nearly undeformed, Fig. 11a), which are probably the defects introduced by the FIB milling during TEM specimen fabrication as well as the sample growth process (Kim et al., 2009). However, many defects-free regions (manifest by the bright contrast) occur in these Nb layers near the pillar top (Fig. 11a), which indicates that most of the defects originally in Nb layers were annihilated by compression. This defect annihilation is consistent with the mechanical annealing of Ni nanopillars observed by *in situ* TEM (Shan et al., 2008). Therefore, the observed dislocation pileup regions near the deformed pillar top are ubiquitously the result of the deformation process rather than FIB-induced artifacts.

Besides, the extrusion of Nb and the nano-cracks formed in the amorphous layer are detected clearly from the HAADF-STEM image (Fig. 11c). However, the interfaces remain intact in the 100 nm sample (Fig. 11c), which means that the deformation of the Nb and amorphous CuNb layers would affect each other rather than deform independently. When the Nb layer is squeezed out between the amorphous layer, it produces shear stress (with the opposite direction to the extrusion) operating in the Nb layer. Correspondingly, the shear stress (with the same direction to the extrusion direction of the Nb layer) works in the amorphous phase. Particularly, the shear

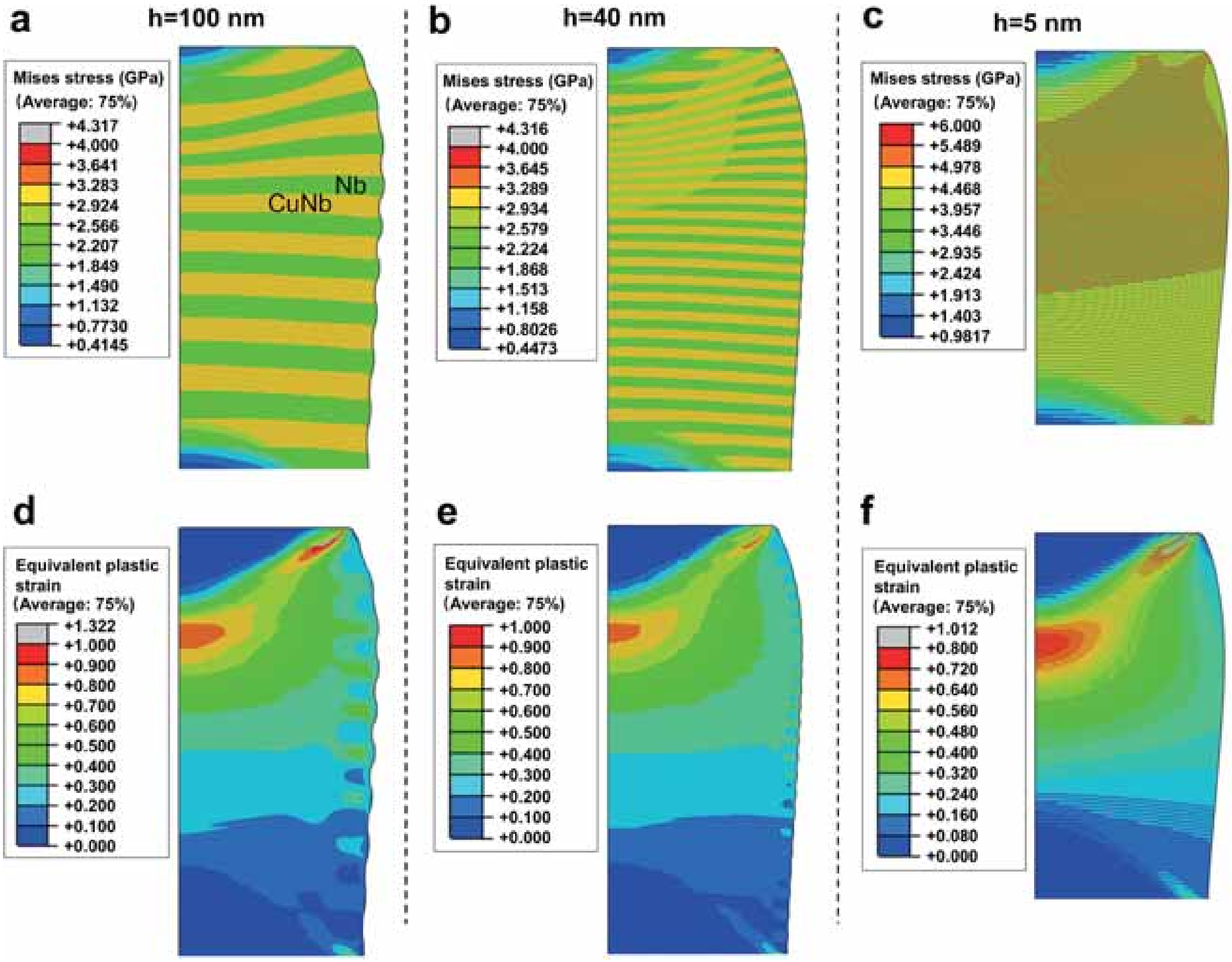

Fig. 12. The simulated deformation configurations of the Nb/CuNb NMFs with different layer thicknesses: (a, d) 100 nm, (b, e) 40 nm, and (c, f) 5 nm, under pillar compression by FE simulations. (a-c) von Mises effective stress of the deformed pillar at 30 % strain. (d-f) Corresponding contour plots of the equivalent plastic strain for the three samples.

stress near the Nb–CuNb interface would be higher than that in the inner layers since the extrusion of the Nb layer is confined by the interface. Therefore, the observed cracks (close to Mode-II cracks) in the amorphous phase can be attributed to the produced shear stress parallel to the interface with the extrusion of the Nb layer, and the brittles of the amorphous phase at a large geometric size above 100 nm (Jang and Greer, 2010).

Fig. 11d shows the plastic strains of Nb and amorphous CuNb layers along the central axis of the pillar. Notably, the strain of the Nb layer is higher than that of the amorphous layer, especially in the severely deformed region, which is quite consistent with the extrusion of Nb layers. These deformation features (layer bending in the pillar top and extrusion of the Nb layer) are further simulated by FE models (the details for FE models can be found in Supplementary Note 1). The FE simulation results show that the constituent layers near the pillar top exhibit a bending toward to the pillar bottom, and the Nb layers are squeezed out between the amorphous CuNb layer (Fig. 12a). It is clear that the plastic strains are concentrated in the pillar top center and pillar top corner (Fig. 12d), which rationalizes that the Nb and CuNb layers were deformed to be more localized near the pillar top regions (Fig. 10b and Fig. 11b).

The employment of the FE simulations is to reproduce the macroscale deformation behavior of the Nb/amorphous CuNb NMF pillars by incorporating the CLS mediated strengthening and deformation mechanism. More details could be obtained by analyzing the strain and stress distribution of the deformed pillars in FE analysis, which are unobtainable in the TEM characterizations. Actually, FE simulations are widely used to simulate the deformation of NMFs under micro/nano-indentations (Chawla et al., 2008; Lee and Chen, 2010; Singh et al., 2011; Tang et al., 2010) and MC tests (Cruzado et al., 2015; Li et al., 2018; Lotfian et al., 2013; Singh et al., 2010). The results of the above studies show that the deformation of the NMFs could be well simulated by FE models if the right micro-mechanism was appropriately included. Therefore, the FE simulation results are reliable, as demonstrated by the good agreement between the simulations and the experimental observations in terms of the extrusion of the soft layers, the barreling of the deformed pillars, and the localized deformation of the constituent layers in the pillar top.

The deformed pillar of the 40 nm sample shows a flat-barrel shape without any shear banding or shear offset under an applied strain of 36.8 % (Fig. 13a), which suggests a stable and homogeneous plastic deformation. In the higher magnification TEM image of the deformed region (Fig. 13b), it can be observed that the Nb and amorphous CuNb layers exhibit a large and homogeneous thinning from 40 nm to 10 nm. The enlarged TEM image of the pillar profile (Fig. 13c) demonstrates no crack formation in the amorphous layers, and the amorphous layers (indicated by the blue triangles) show a homogenous plastic deformation and slight extrusion as compared to the

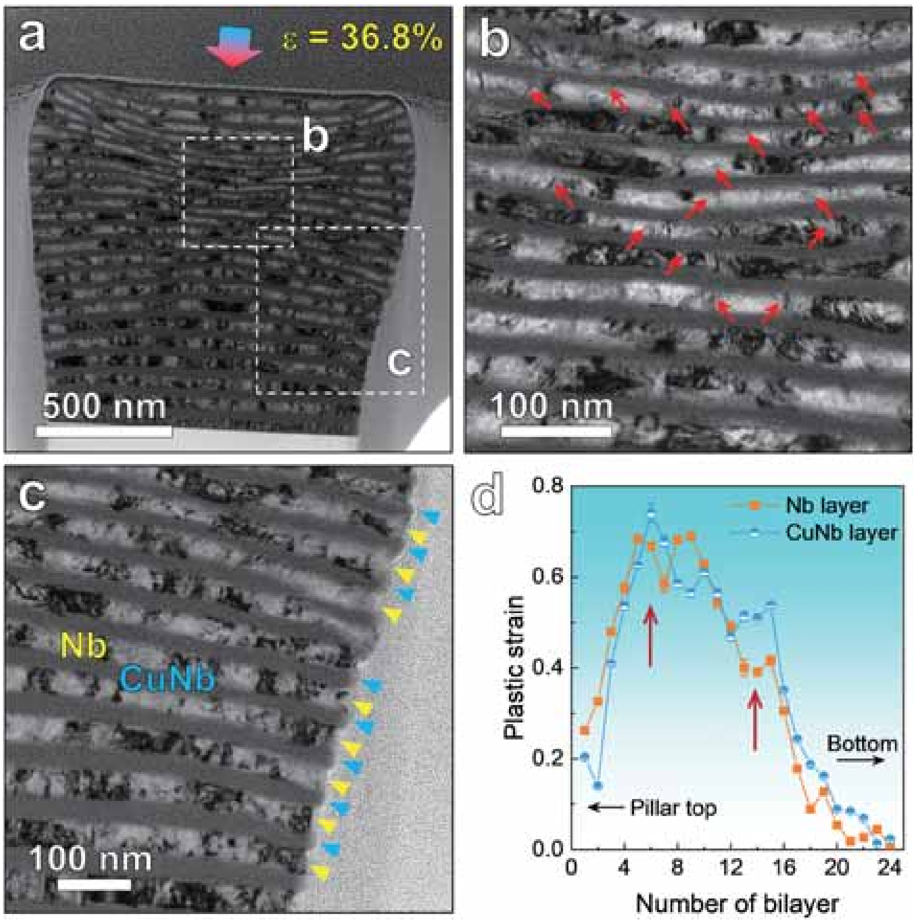

Fig. 13. Microstructures of the deformed pillar (D = 849 nm) under an applied strain of 36.8 % for the 40 nm sample. (a) Cross-sectional bright-field TEM image. (b) High-magnification TEM image of the severely deformed region. (c) Enlarged image of the pillar side. (d) Plastic strains of the Nb and amorphous CuNb layers from the pillar bottom to the top along the pillar axis, as calculated from the measurements of the change of the layer thickness before and after deformation from (a).

Nb layers (indicated by the yellow triangles). The slight extrusion of the amorphous CuNb layer may originate from the size-dependent strength of the Nb layers and the size-independent one of the amorphous layers. According to the CLS model, the strength of the crystalline nanolayer is continuously increasing with the decrease of the layer thickness. Then, the corresponding flow stress of the Nb layer with layer thickness of 10 nm is 3.16 GPa, as given in our previous work (see Fig. 15 in Qin et al. (2024)), which is higher than the flow strength of the amorphous CuNb layer (3.13 GPa). The extrusion occurs in the softer layer of the NMFs under the pillar compression-induced isostress state. Besides, the plastic strains of the bilayers in the 40 nm sample show a "double-barrel" shape (designed by arrows in Fig. 13d) as distinguished from the one-barrel shape observed in the 100 nm sample (Fig. 11d), which indicates the strain is delocalized in the pillar of the 40 nm sample. Under a higher applied strain of 48.5 %, the pillar also exhibits a similar homogeneous deformation without cracks or SBs (Figs. 14a–d). Hence, $\varepsilon_{\mathrm{HDS}}^{\mathrm{MC}} = 48.5\,\%$ is obtained for the 40 nm sample.

Moreover, plentiful thin-striped dark regions can be observed in the bright-field TEM images (indicated by red arrows in Fig. 13b and Fig. 14b) of the deformed pillar. The HRTEM observations further reveal some deformation twins in the dark regions as shown in Figs. 15a–f. Fig. 15b shows the coherent twin boundary (TB) on the {112} plane with a step of one (112) layer (with 1/6<111> Burgers vector). Similar deformation twins have also been reported in coarse-grained BCC Nb, Ta (Jiang et al., 2018) and tungsten nanowires (Wang et al., 2022). Another deformed region indicates both twin and twin island formation in the BCC Nb layer (Fig. 15d). The SAED pattern (inset in Fig. 15d) suggests the overlap of the matrix and the twin lattices in the twin island. However, the TBs with stepwise shown in Fig. 15e are located between two {112} atomic planes, which is different from the typical coherent TB where the TB atoms belong to the lattices of both the matrix and the twin. This kind of TB was called isosceles-type TB, as first proposed by Vítek (1970). The recent *in-situ* TEM tensile experiments conducted by Zhao et al. (2023) also revealed the co-existence of both coherent and isosceles TBs in Fe nanowires. The formation of isosceles-type TB may be attributed to the dissociation of 1/6<111> twinning dislocation in the reflection symmetric TB into two equal 1/12<111> partials, which subsequently glides on two adjacent planes to realize isosceles twinning (Bristowe and Crocker, 1975; Faisal and Weinberger, 2023; Zhao et al., 2023). As a consequence, the CLS dislocation mechanism and the deformation twinning activated in BCC crystalline Nb in the 40 nm sample promote the co-deformation between the crystalline layer and the amorphous one. This co-deformation is also revealed by the FE simulation (Fig. 12b) due to the reduced strength differences between the Nb layer and the amorphous layer. Meanwhile, the amorphous layers also undergo a homogenous plastic flow since the propagation of the SB is inhibited at such a small space (< 100 nm) (Guo et al., 2007; Jang and Greer, 2010).

In order to uncover the evolution of the deformation twinning and the underlying differences in mechanical responses between

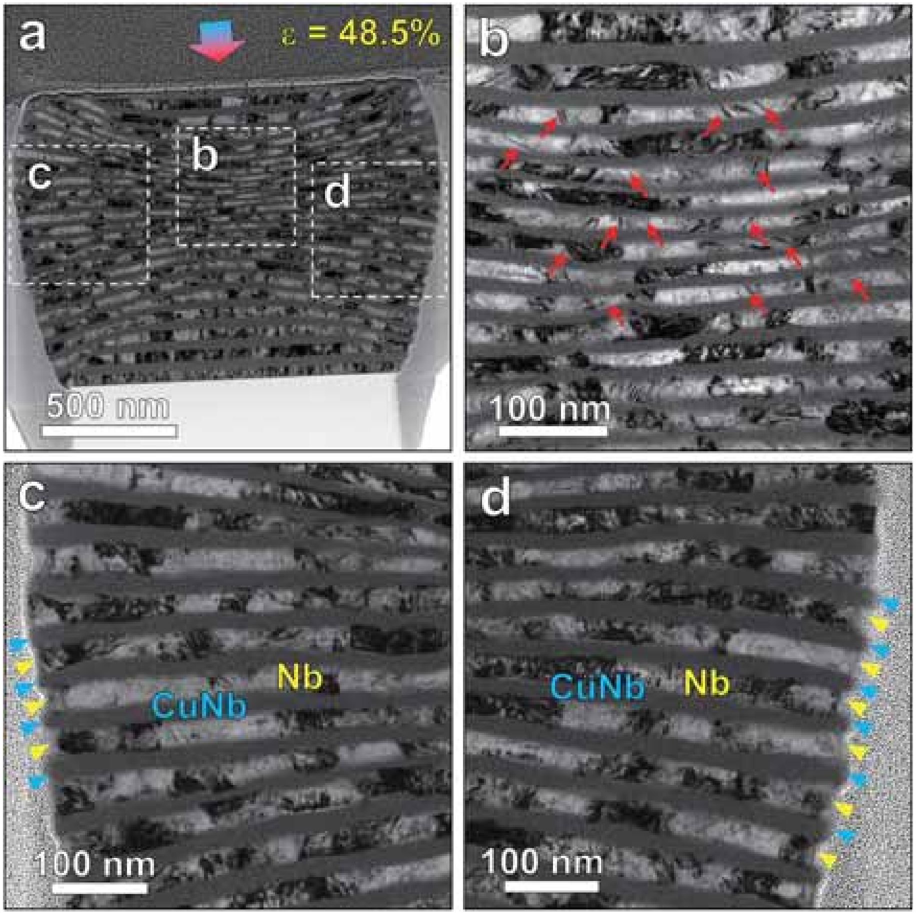

Fig. 14. TEM microstructures of the deformed pillar ($D = 859$ nm) under an applied strain of 48.5 % for the 40 nm sample. (a) Bright-field TEM image. (b) Magnified TEM observation of pillar centra. (c) and (d) are the TEM images of the pillar left and right sides, respectively.

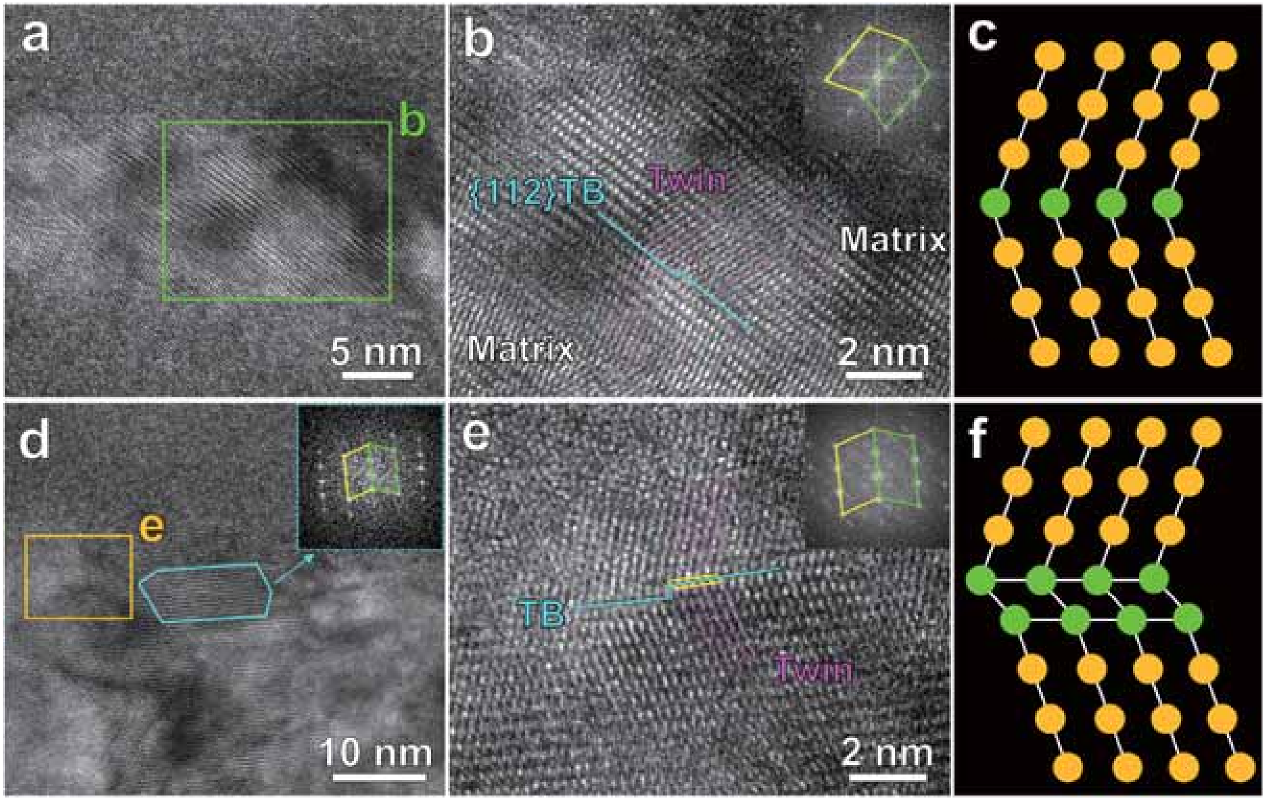

Fig. 15. Deformation twinning in the deformed pillar of the Nb/amorphous CuNb NMF with layer thickness of 40 nm. (a) HRTEM image of a deformed region that contains the deformation twin in the Nb layer. (b) Atomic-level image of the deformation twin viewed along [111] zone axis. (c) Atomic configuration of the observed twin boundary (TB) in (b). (d) HRTEM image of another deformed region that contains twin and twin island (outlined by the irregular box) in the Nb layer. The inset in (d) is the FFT pattern of the twin island. (e) Atomic observation of the twin structure taken from (d). (f) Atomic configuration of the observed TB in (e). The insets in (b) and (e) are the corresponding FFT patterns, respectively.

tensile and compressive loadings, MD simulations were performed to investigate the tensile and compressive deformation behaviors, where the loading is applied parallel to the layer interface in the former and perpendicular in the latter. The atomic model of the Nb/amorphous CuNb NMF sample is depicted in Supplementary Fig. 8, in which the 10 nm Nb layer and 10 nm amorphous CuNb layer are stacked alternately along the *y*-direction. The initial orientations of Nb layers were set to be $x = [1–12]$, $y = [110]$, $z = [−111]$ according to the experimentally observed orientations for the Nb layer in NMFs prepared by magnetron sputtering (Chen et al., 2020c). Also, these orientations have been valid for describing the mechanical response of the BCC crystalline Nb layer (Jian et al., 2022). A "melt-quench" method (Cheng and Trelewicz, 2016; Zhou et al., 2014) was employed to obtain the amorphous structures of the $Cu_{60}Nb_{40}$ layers. The more details about the MD simulations are described in Supplementary Note 2.

Fig. 16a shows the stress–strain curve of the sample under tension in the *x*-direction. The stress increases linearly with the applied strain as the strain increases from 0 to 11 %, presenting an elastic stage. Subsequently, the stress decreases sharply until the strain is up to 12 %. The stress drop is induced by the plastic deformation, i.e., dislocation nucleation and deformation twinning (Fig. 16c). After that, the stress tends to be stable. A similar elastic stage exists in the sample under compression in the y-direction, which is followed by a sharp stress drop (Fig. 16e) and the deformation twining (Fig. 16g). The stress shows continuous increases with increasing strain until the strain reaches 17.4 %. New dislocation nucleation and propagation occur in response to the increased stress, resulting in a second stress drop. The stress tends to be stable at higher strain because the deformation is accommodated by the dynamic process of dislocation generation/annihilation (Fig. 16h). The atomic configuration of the twin shows a mirror symmetry respective to the TB with 1–2 atomic steps (red dashed lines), as shown in Supplementary Fig. 9, which is consistent with the observed coherent TB in the 40 nm sample (Fig. 15b). Besides, the twin lamellae are continuously thickened with the straining process both in tensile (Figs.16c and d) and compressive (Figs. 16g and h) loadings. This may be attributed to that BCC metals generally have much higher twin nucleation energies but relatively lower twin thickening barriers (Li et al., 2010a). Therefore, the twin lamellae can further thicken from other locations, such as steps on the TBs where the local stress is easily concentrated and built up for the thickening, as schematized in Fig. 16i. This twin-thickening process is similar to the growth of deformation twinning reported in BCC Ta under *in situ* TEM tensile test and MD simulations (Jiang et al., 2018). Notably, the stress–strain responses of the Nb/CuNb NMFs under tensile and compressive loadings are quite different. This presumedly originates from the anisotropy of the loading orientation, as reported in other NMFs, e.g., Cu/Nb (Cheng et al., 2024), Cu/Fe and Al/Fe (Zhang et al., 2024) systems. The above MD simulations demonstrate the consistency of the deformation mechanism of the Nb/CuNb NMFs under compressive and tensile loadings, even though the stress–strain response differs between these two different loading modes.

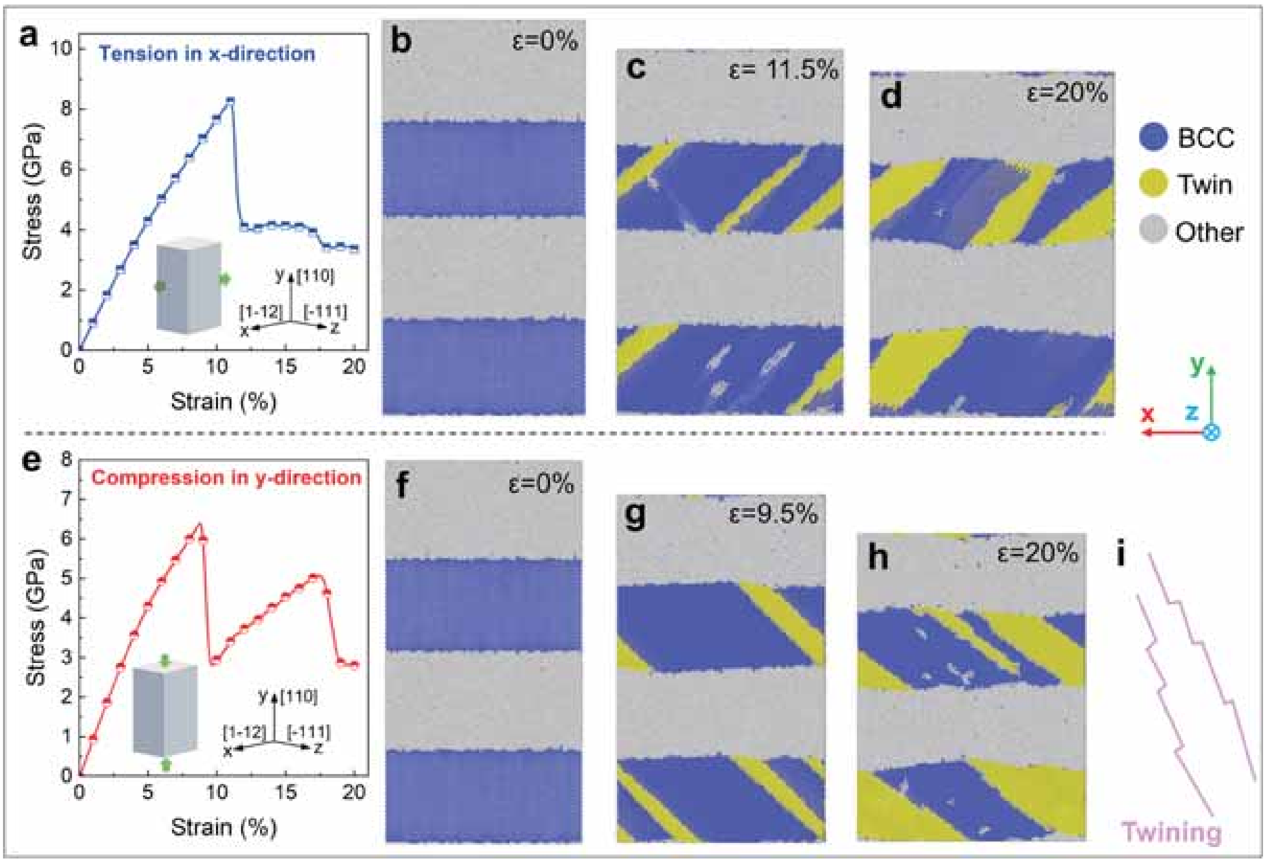

Fig. 16. MD simulations of the Nb/amorphous CuNb NMF with layer thickness of 10 nm under tensile and compressive loadings. (a) The stress–strain response and (b-d) microstructure evolution of the sample under tension in *x*-direction, i.e., parallel to the interface. (e) Stress–strain curves and (f-h) corresponding microstructure evolution with strain processed for the same sample the compression in *y*-direction (perpendicular to the interface). (i) Schematic illustration of the twin lamella structure, where the pink lines represent the TB.

It should be noted that the performing of the tensile tests in experiments is out of the scope of the present study and can be performed in the future. Different from the conventional mechanical tensile test for bulk materials, the uniaxial tension for film samples with thickness around micrometers can be achieved via *in-situ* tensile tests in TEM (Zhang et al., 2020a). According to the reported *in situ* TEM tension for NMFs, the deformation mode was commonly governed by crack nucleation and growth, as reported in Cu/Nb (Liu et al., 2018) and CrCoNi/TiZrNbHf (Wu et al., 2021) NMFs. Due to the early crack nucleation, the elongation of film under tensile test is generally lower than 10 % (Beyerlein et al., 2012; Liu et al., 2018). For example, the onset of cracking happens at an applied strain of 8 % in a 63 nm Cu/Nb NMF under tensile loading parallel to the layer interface (Liu et al., 2018).

Fig. 17 presents the microstructures of the deformed pillar for the 5 nm sample under an applied strain of 20.9 %. From the bright-field TEM images (Figs. 17a and b), the pillar shows a homogeneous deformation without cracks or SBs. The SAED patterns of the less (Fig. 17c$_1$) and severely deformed (Fig. 17c$_2$) regions both indicate the strong Nb (110) texture without obvious amorphization. Note that only a shear step occurs in the deformed pillar under an applied strain of 31.6 % (Fig. 8c$_2$). However, a shear offset (denoted by the red arrow) can be observed in the pillar under a higher applied strain of 43.3 % (Fig. 18a). This shear offset corresponds to the SB observed in the SEM image of the deformed pillar (Fig. 8c$_3$). Thus, the applied stain of 31.6 % is approximated as the HDS, i.e., $\varepsilon_{\mathrm{HDS}}^{\mathrm{MC}} = 31.6\,\%$ for the 5 nm sample. A high-magnification TEM image (Fig. 18b) indicates that the layered structure failed to be identified in the pillar middle section due to the severe strain localization in this region, as demonstrated by FE simulation (Fig. 12f). The SAED pattern (Fig. 18b$_2$) of the pillar middle (red circle) shows an amorphous ring instead of the crystalline spots as detected in the less deformed region (Fig. 18b$_1$), which suggests that the BCC crystalline layer may be amorphized to some extent and mixed with the amorphous layer in the severely deformed region. Moreover, it can be seen that the SB initiates from the severely deformed region and propagates along the maximum shear stress plane (45° to the load axis), as outlined by the white dash lines in Fig. 18c. Furthermore, the HRTEM image (Fig. 18d) further reveals the mixed nanocrystalline (dark contrast) with a grain size of 2–11 nm in width and amorphous phase (bright contrast) with a thickness of 2–8 nm within the SB region. As a result, the shear banding in the 5 nm sample originates from the strain localization-induced interface failure, which in turn produces a thick amorphous-like region for the nucleation of the SB.

Recently, Zhang et al. (2024) showed that the interface strength of NMFs plays a significant role in the development of shear instabilities under MC which represents an isostress loading condition. Shear localization in the form of interface sliding/shearing or across several layers (shear banding) is expected to occur in NMFs with weak interface strength, as observed in 50 nm Cu/Fe and Ag/Fe systems (Zhang et al., 2024). For the present Nb/CuNb NMFs, no delamination and interface sliding/shearing were detected during MC

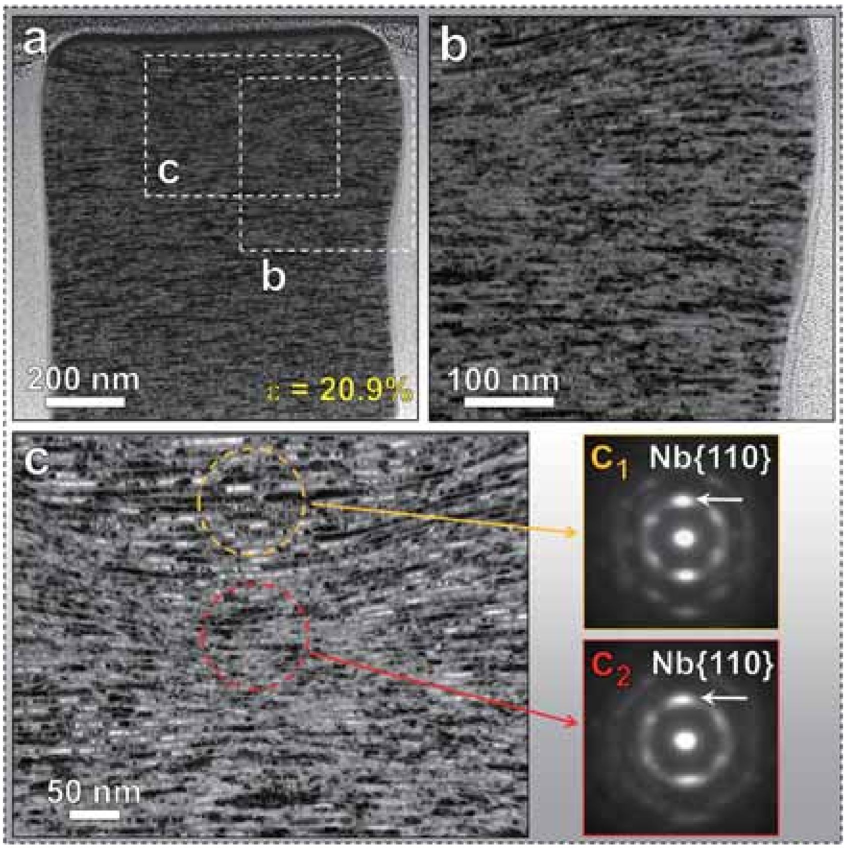

Fig. 17. TEM observations of the pillar ($D = 667$) under an applied strain of 20.9 % for the 5 nm sample. (a) Bright-field TEM image. (b) Enlarged TEM image of the pillar side. (c) High-magnification TEM image of the pillar center. (c_1) and (c_2) are the SAED patterns of the less deformed and the severely deformed regions, respectively.

in all samples, which indicates the strong strength of the Nb-CuNb interface. For example, the interfaces remain intact under a large applied strain of 36.1 % in the 100 nm sample though there appears slight extrusion of Nb layers (Fig. 11c). The strong interface strength of the Nb/CuNb NMFs possibly arises from the atomic intermixing between Cu and Nb at the interface region (Fig. 2b), which enhances the cohesive strength of the interface (Vo et al., 2012).

3.4. MI-induced deformation of the Nb/CuNb NMFs

The MI tests for the three Nb/CuNb samples have been conducted in our previous study (Qin et al., 2024). Here, only essential results and findings are presented for the sake of the development of an effective strain-based approach to quantitatively evaluate the plasticity of the thin films by MIs. The typical MI-induced deformation behavior of the Nb/CuNb samples is presented in Fig. 19. From the SEM image of the micro-indents, profuse circle-shaped pileups can be observed around the indent of 100 nm (Fig. 19a) and 5 nm (Fig. 19c) samples. Extensive studies (Li et al., 2022, 2010b; Qin et al., 2024) have demonstrated that these circle-shaped pileups result from severe shear banding inside the material. Only slight pileups have been observed in the 40 nm sample (Fig. 19b), which suggests the shear banding is suppressed in the 40 nm sample. The microstructures under the micro-indent (Figs. 19d–f) clearly show that the SBs in the 100 nm (Fig. 19d) and 5 nm (Fig. 19f) samples are all mediated by the cooperative kinking of almost all the constituent layers. However, a homogeneous deformation without SBs has been discovered in the 40 nm sample, as seen from the cross-sectional STEM image (Fig. 19e and Supplementary Fig. 3e). The appearance of the slight pileup in the indented surface of the 40 nm sample comes from the constraint of the indenter and the substrate during deformation instead of the shear banding. Similar pileups have also been observed in monolayer metallic film where no shear banding occurs, e.g., Nb film (Qin et al., 2024).

In order to quantitatively compare the shear banding-mediated surface pileup in the three samples, the shear displacement (h_d) produced by the SB, as illustrated in Fig. 19g, has been measured. The values of h_d for the 100 nm and 5 nm samples can be obtained from the cross-sectional STEM images (Supplementary Fig. 3d and f), which are determined as 96.5 nm for the 100 nm sample and 135.4 nm for the 5 nm one (Fig. 19h). The h_d for the 40 nm sample is zero because of the completely suppressed shear banding (Fig. 19e and Supplementary Fig. 3e). Our previous work (Qin et al., 2024) has shown that the shear banding was also detected in two representative intermediate thicknesses ($h = 65$ nm and $h = 20$ nm samples), demonstrating the best plasticity gained in the 40 nm one among all the studied samples. Besides, the MCs also reveal excellent deformability at $h = 40$ nm, as demonstrated by a HDS of 48.5 %. In contrast, nano-cracks are observed in the 100 nm at an applied strain of around 20 % and shear banding-induced failure occurred in the 5 nm sample at an applied strain of around 30 %. Consequently, these findings indicate the optimum layer thickness is 40 nm

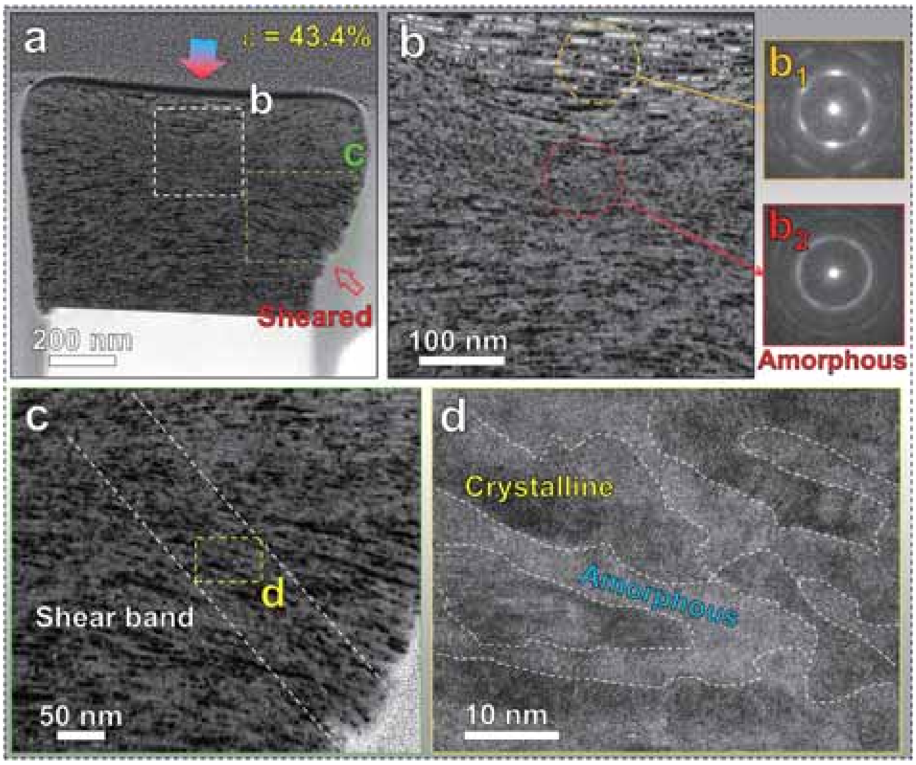

Fig. 18. Cross-sectional TEM microstructures of the deformed pillar ($D = 650$ nm) under an applied strain of 43.4 % for the 5 nm sample. (a) Bright-field TEM image. (b) Enlarged TEM observation of the pillar center. (b_1) and (b_2) indicate the SAED patterns of the less deformed and the severely deformed regions, respectively. (c) TEM image of pillar side. (d) HRTEM micrograph taken from the SB region, showing the mixed nanocrystalline and amorphous phases with the destroyed layer interface.

among all the investigated samples, at which the Nb/CuNb NMFs achieve the best plasticity.

3.5. *Quantitative correlation between the MC and MI-measured plasticity*

The above results clearly show that both the MC and MI tests demonstrated a strong non-monotonical layer thickness dependence in the deformation behaviors of the Nb/CuNb NMFs, revealing an optimal deformability and plasticity in the 40 nm sample. In this section, an effective strain-based theoretical model is developed to quantitatively evaluate the plasticity of the Nb/CuNb films by incorporating the MI-induced complex 3-D stress state. The MI-derived plasticity is then directly compared with the MC-measured one. Note that the MC-measured HDSs ($\varepsilon_{\mathrm{HDS}}^{\mathrm{MC}}$) are 21.2 %, 48.5 % and 31.6 % for the 100 nm, 40 nm and 5 nm samples, respectively. Here the $\varepsilon_{\mathrm{HDS}}^{\mathrm{MC}}$ values for the three samples are measured from the small pillars with TEM characterizations being conducted for the deformed counterparts, because it is a formidable task to characterize all the deformed small and big pillars under different applied strains by TEM in order to measure the HDS by checking the SB and micro-/nano-cracks. Actually, it is not a necessity to do all the characterizations since the mechanical responses of these pillars with different diameters for the same sample do not vary significantly, as shown in the stress–strain responses (Fig. 5).

In order to give a direct quantitative comparison between the MC-measured plasticity and the MI-measured one for the Nb/amorphous CuNb NMFs, the previous theoretical model (Qin et al., 2024) has been extensively extended here to incorporate the three-dimensional stress state as produced by the MI tests. To give a quantitative description on the MI-measured plasticity of thin films, the deformation problem under MI is simplified to be an axisymmetric one considering that the indent geometry and the applied force conditions produced by the MI are both symmetric to the loading axis, i.e., z-axis, as schematized in Fig. 20a. The MI-induced deformation areas can be divided into two regions, i.e., the shear banding region (region 1) that bears the most of the strains under the applied load due to the shear banding induced strain localization, and the region outside the SB (region 0) that undertakes much less strains, as illustrated in Fig. 20b.

The deformation of each layer under MIs can be represented by that of a microelement. Then, the strain differences between region 1 and region 0 can be used to quantify the magnitude of the strain localization in the *i*-th layer, i.e.,

$$\Delta\varepsilon_i = \varepsilon_i^1 - \varepsilon_i^0 \tag{2}$$

where ε_i^1 and ε_i^0 denote the effective strain in the shear banding region and the region outside the shear banding area, respectively. The effective strain can be expressed as

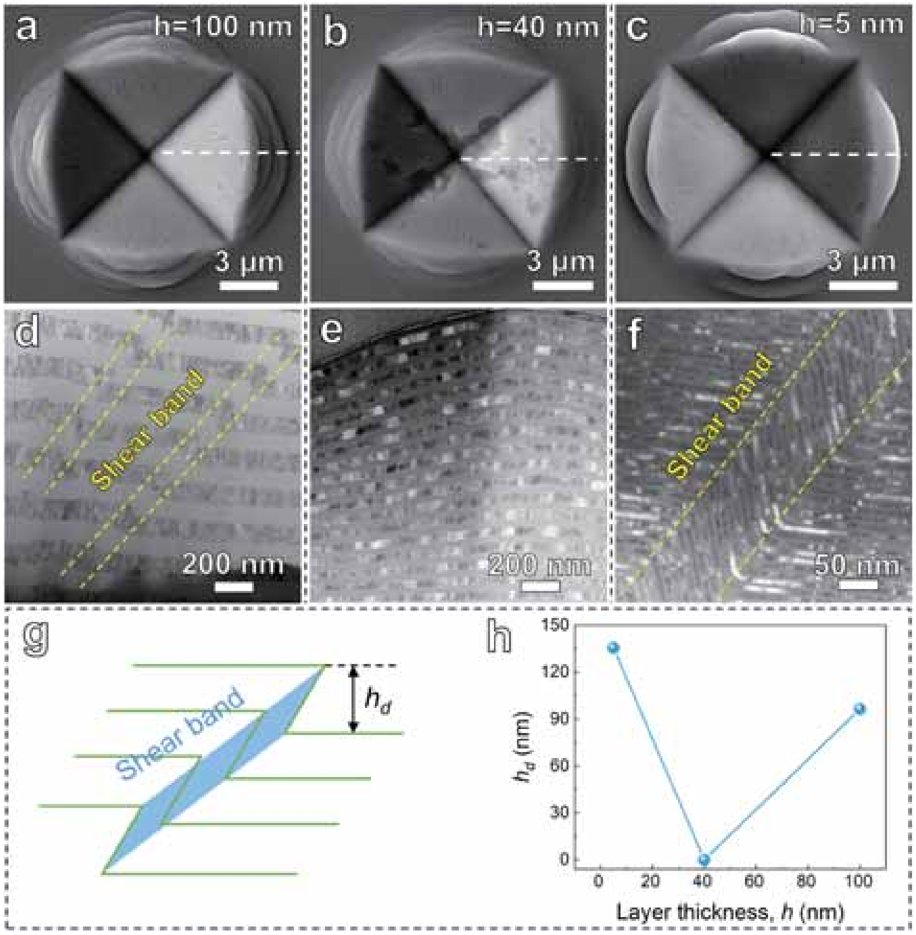

Fig. 19. The MI-induced deformation in the Nb/amorphous CuNb NMFs with different layer thicknesses, i.e., (a, d) 100 nm, (b, e) 40 nm and (c, f) 5 nm. (a–c) SEM images of the micro-indent morphology under a load of 50 g. (d–f) Corresponding cross-sectional dark-field STEM images of the micro-indents, in which the green arrows indicate the position of the Vickers indenter. The dash lines in (a–c) indicate the position of the TEM lamellas that were taken. (g) Schematic of the SB-induced displacement in the indented surface (h_d). (h) The variation of h_d with respect to the layer thickness.

$$\varepsilon_i = \frac{\sqrt{2}}{3}\sqrt{(\varepsilon_z-\varepsilon_r)^2+(\varepsilon_z-\varepsilon_\theta)^2+(\varepsilon_r-\varepsilon_\theta)^2+\frac{3}{2}\gamma_{rz}^2} \tag{3}$$

in which ε_z, ε_r and ε_θ are the strain components in the axial, radial and circumferential directions, respectively. γ_{rz} represents the shear strain component induced by the displacements in the axial and radial directions. Due to the axial symmetry, $\gamma_{z\theta}$ and $\gamma_{r\theta}$ are zero.

The deformed microstructures (Fig. 19) have shown that the region 0 is deformed almost homogeneously in uniaxial direction and the deformation is usually much less than that of the region 1. Hence, the only non-trivial strain components are the three normal strains. Here for simplicity, it is assumed that the trivial strain components in region 0 can be ignored without causing significant errors. As a result, the effective strain in the region 0, ε_i^0, is now equal to the absolute value of the normal strain in the compression direction, which can be calculated by the change in the layer thickness before and after deformation in region 0, that is

$$\varepsilon_i^0 = \left|\varepsilon_z^0\right| = \frac{h_b - h_{a,i}^0}{h_b} \tag{4}$$

here h_b is the original layer thickness, and $h_{a,i}^0$ represents the thickness of the i-th layer within region 0 after deformation.

According to the deformation geometric feature of the layer within the shear banding region (Fig. 20c), the normal strain in the axial direction for the i-th layer can be calculated as:

$$\varepsilon_z^1 = \frac{h_{a,i}^1 - h_b}{h_b} \tag{5}$$

in which $h_{a,i}^1$ represents the thickness of the i-th layer within the shear banding region (region 1) after deformation. The normal strain in the radial direction can be calculated as:

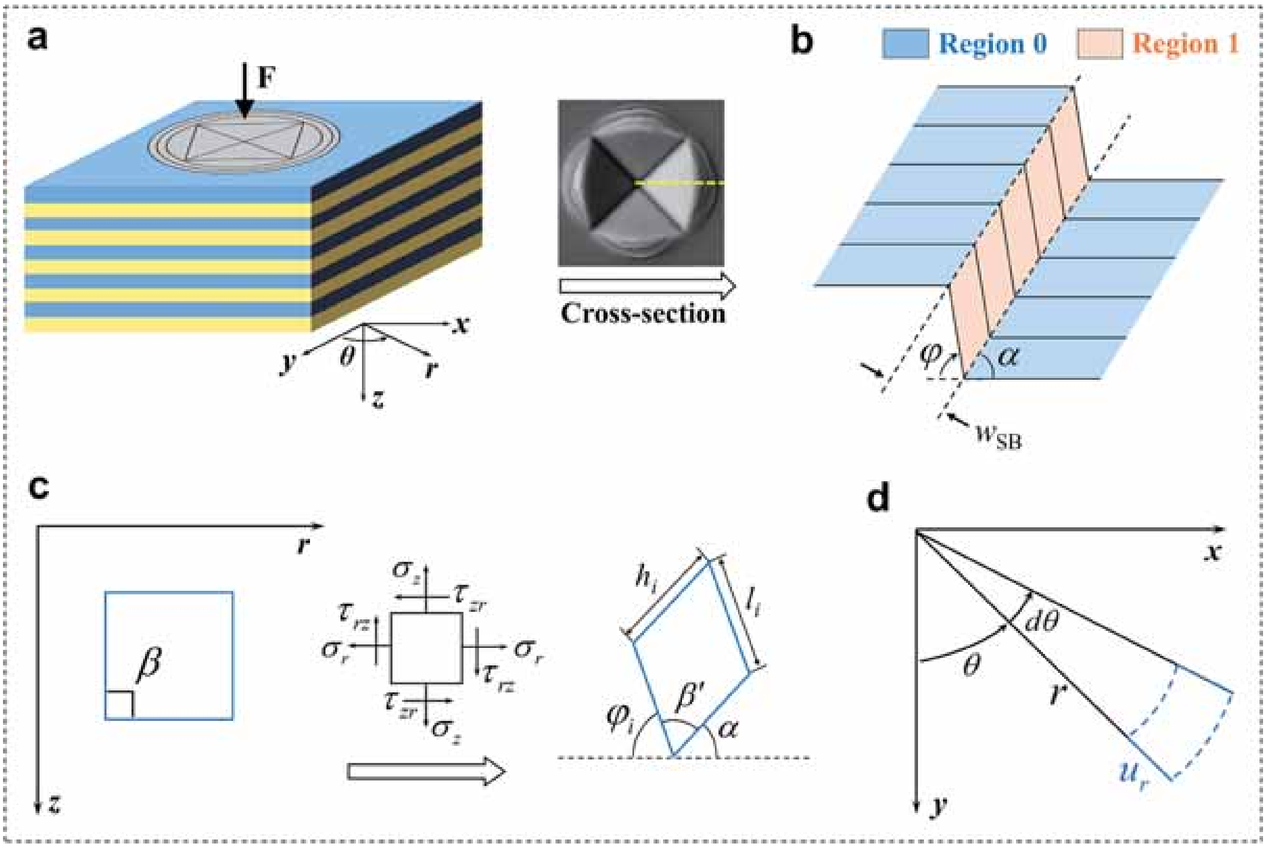

Fig. 20. The theoretical model that describes the MI-induced deformation. (a) Schematic representation of the micro-indent made in a nanolayered sample. (b) Schematic illustration of the cross-sectional deformation morphology of the micro-indent, including the shear banding region (region 1, orange) and the region outside the shear banding region (region 0, blue). The SB is outlined by the dashed lines, where w_{SB} and α are the width and tilt angle of the SB, respectively. φ is the kink angle of the interface inside the SB. (c) The deformation and stress state of the microelement induced by the axial and radial displacements. (d) Schematic of circumferential elongation induced by the radial displacement (u_r).

$$\varepsilon_r^1 = \frac{l_i - l}{l} \tag{6}$$

where l and l_i indicate the length of the layer that is parallel to the horizontal interfaces before and after deformation, respectively. l_i can be measured in the shear banding region. l is determined by $w_{\mathrm{SB}}/\sin\alpha$ according to the geometric relation, where w_{SB} denotes the SB width and α is the tilt angle of the SB. The normal strain in the circumferential direction can be derived by assuming that the MI-induced deformation is small, and is thus expressed as:

$$\varepsilon_\theta^1 = \frac{u_r}{r} \tag{7}$$

here u_r represents the radial displacement. Eq. (7) can be re-written as:

$$r\varepsilon_\theta^1 = u_r \tag{8}$$

By differentiating Eq. (8) with respect to r, we have:

$$\varepsilon_\theta^1 + r\frac{\partial \varepsilon_\theta^1}{\partial r} = \frac{\partial u_r}{\partial r} = \varepsilon_r^1 \tag{9}$$

It is noted the strain in the shear banding region is highly localized and almost homogeneously. Hence, the strain gradient, i.e., $\partial\varepsilon_\theta^1/\partial r$ in Eq. (9) is very small and can be assumed to be zero for the sake of simplicity without losing the physical feature of the deformation problem. In this case, we have,

$$\varepsilon_\theta^1 = \varepsilon_r^1 \tag{10}$$

The shear strain component γ_{rz}^1 can be calculated based on the change in the right angle of the microelement (Fig. 20c), which is also derived based on the assumption of small deformation in our previous work (Qin et al., 2024):

$$\gamma_{rz}^1 = \beta - \beta' = \alpha + \varphi_i - \frac{\pi}{2} \tag{11}$$

where φ_i is the interface kink angle of the i-th layer within the shear banding region. Now the effective strain of the i-th layer in region 1 becomes

$$\varepsilon_i^1 = \frac{\sqrt{2}}{3}\sqrt{2\left(\varepsilon_z^1-\varepsilon_r^1\right)^2+\frac{3}{2}\left(\gamma_{rz}^1\right)^2} = \frac{2}{3}\sqrt{\left(\frac{h_{a,i}^1}{h_b}-\frac{l_i\sin\alpha}{w_{\mathrm{SB}}}\right)^2+\frac{3}{16}(2\alpha+2\varphi_i-\pi)^2} \tag{12}$$

The $\Delta\varepsilon_i$ value of different constituent layers is different due to the varying shear and normal strain components in each layer and the bigger the $\Delta\varepsilon_i$ value, the higher the strain localization. Hence, the maximum $\Delta\varepsilon_i$ value in all the constituent layers, i.e., $\Delta\varepsilon_m$, can be used to represent the degree of strain localization of this sample under MIs. That is, the higher the $\Delta\varepsilon_m$ value, the lower the plasticity of the thin films. In order to directly compare with the plasticity given by MCs ($\varepsilon_{\mathrm{HDS}}^{\mathrm{MC}}$), a similar HDS is defined here to quantify the MI-measured plasticity, i.e.,

$$\varepsilon_{\mathrm{HDS}}^{\mathrm{MI}} = \varepsilon_{\mathrm{HDS}}^{l} - \Delta\varepsilon_m \tag{13}$$

where $\varepsilon_{\mathrm{HDS}}^{l}$ denotes the limit value of the $\varepsilon_{\mathrm{HDS}}^{\mathrm{MI}}$ that the sample can reach. Note that the Nb/CuNb NMFs achieved a homogeneous deformation without shear banding at $h = 40$ nm under MI with an applied load of 50 g. In this case, the shear banding region disappears, and we have $\varepsilon^1 = \varepsilon^0$ for the 40 nm sample and in turn $\Delta\varepsilon_m = 0$. Therefore, it is obtained that $\varepsilon_{\mathrm{HDS}}^{l} = \varepsilon_{\mathrm{HDS}}^{\mathrm{MI}} = \varepsilon^1 = \varepsilon^0$ for the 40 nm sample since it exhibits homogeneous deformation under the given load. This $\varepsilon_{\mathrm{HDS}}^{l}$ value is also adopted for the 100 nm and 5 nm samples because it represents the best plasticity among all these samples. It is clear from Eq. (13) that the higher the $\varepsilon_{\mathrm{HDS}}^{\mathrm{MI}}$ value, the better the plasticity, which now can be employed to directly compare with the HDS obtained by the MC tests.

The value of the parameter $h_{a,i}^0$ in Eq. (4) for the 40 nm sample was determined to be the average thickness of the deformed layers, i.e., 24.1 nm, whereas h_b is the original layer thickness of the as-deposited 40 nm sample, i.e., 39.1 nm, which was measured from the cross-sectional TEM image of the as-prepared film (Fig. 2a). As for the 5 nm and 100 nm samples, the strain difference $\Delta\varepsilon_m$ can be calculated in the constituent layer with the maximum interface kink angle ($\varphi_{\max}$) before interface failure. In particular, the $\varphi_{\max}$ value should be lower than π/2 for the 100 nm sample, because the layer shows a cutting-like shape when $\varphi > \pi/2$ which is considered as an interface failure, as observed in the 100 nm sample (Fig. 19d). Other parameters including SB width (w_{SB}) and tilt angle of the SB (α) can be measured from the STEM images (Figs. 19d and f), while the $h_{a,i}^0$ was measured from region 0 (near the shear banding region) in the layer that reaches $\varphi_{\max}$ inside the SB. Based on all these measured parameters (Table 1), the $\varepsilon_{\mathrm{HDS}}^{\mathrm{MI}}$ values are calculated to be 14.4 % for the 100 nm sample, 38.4 % for the 40 nm sample and 26.9 % for the 5 nm one. The above values are in quantitatively good agreement with the HDSs determined by MCs, i.e., $\varepsilon_{\mathrm{HDS}}^{\mathrm{MC}}$, which are 21.2 % for the 100 nm sample, 48.5 % for the 40 nm sample and 31.6 % for the 5 nm one, as presented in Fig. 21. The slightly lower values based on the proposed approach than the MC-measured ones might be attributed to that the limit value of the HDS, i.e., $\varepsilon_{\mathrm{HDS}}^{l}$ for the 40 nm sample, has been underestimated because no SB was formed in this sample even under the applied load of 50 g in MI tests. The above findings demonstrated that the plasticity of the NMFs can be quantitatively evaluated by MI tests with the aid of the newly developed theoretical model at least for the first approximation, and that the evaluation is in acceptable agreement with the MC measured one.

Finally, the size-dependent mechanical properties of the Nb/CuNb NMFs are summarized in Fig. 22, in which the corresponding data for other NMFs in existing studies are included for comparison. It can be found that the Nb/CuNb NMFs exhibit a better balance of strength-plasticity as compared with other reported NMFs, such as Cu/amorphous CuZr (Zhang et al., 2012c), multilayers with 3D interface (Chen et al., 2020c; Cheng et al., 2022) and multilayer with high entropy component (Wu et al., 2021), suggesting the ductile BCC crystalline-amorphous NMFs for promising structural applications in micro/nano-scale systems. It should be indicated that the extrinsic size effect (pillar diameter) on the yield strength and HDS of the Nb/CuNb NMFs is not significant when the pillar is enlarged by about 30 % for the 100 nm and 40 nm samples, and about 20 % for the 5 nm sample, as shown and discussed in Section 3.3. Therefore, the obtained yield strength and homogeneous deformation in this study can be compared with these existing data, although part of these data originates from larger pillars than this work. Although the data listed in Fig. 22 for existing crystalline/amorphous NMFs may not be exhaustive, to the best knowledge of the authors, they encompass almost all the representative crystalline-amorphous systems that have been widely explored by researchers, including FCC-amorphous systems (e.g., Cu/CuZr, Cu/CuNb), BCC-amorphous systems (e.g., Ta/ZrCuTi), etc., aiming to give a comprehensive comparison with the present BCC Nb/amorphous CuNb NMFs.

It should be pointed out that there are several important and necessary assumptions and simplifications as adopted in the proposed theoretical model as summarized as follows, without losing the physical feature of the MI deformation that produces complex 3-D stress state. The first assumption is that the MI-induced deformation is assumed to be an axisymmetric problem in order to derive

Table 1
The measured geometric parameters within the deformation region under MIs for the Nb/CuNb NMFs.

Samples	h_b (nm)	$h^0{}_{a,i}$ (nm)	α (degree)	$\varphi_{\max}$ (degree)	w_{SB} (nm)	$h^1{}_{a,i}$ (nm)	l_i (nm)
$h = 100$ nm	92.8	80.9	49	84	33.8	82.5	66.7
$h = 40$ nm	39.1	24.1	/	/	/	/	/
$h = 5$ nm	4.1	3.6	53	81	109.0	3.4	130.0

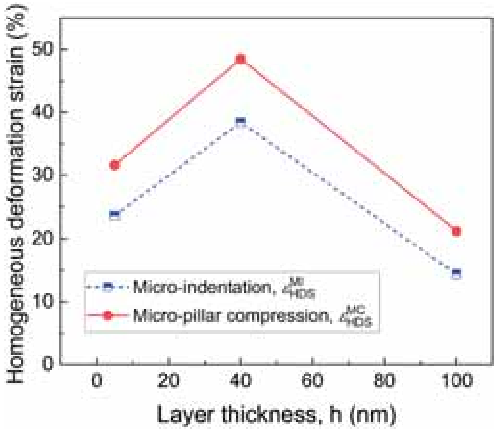

Fig. 21. The HDSs of the Nb/CuNb NMFs determined by MC ($\varepsilon_{\mathrm{HDS}}^{\mathrm{MC}}$) and MI ($\varepsilon_{\mathrm{HDS}}^{\mathrm{MI}}$).

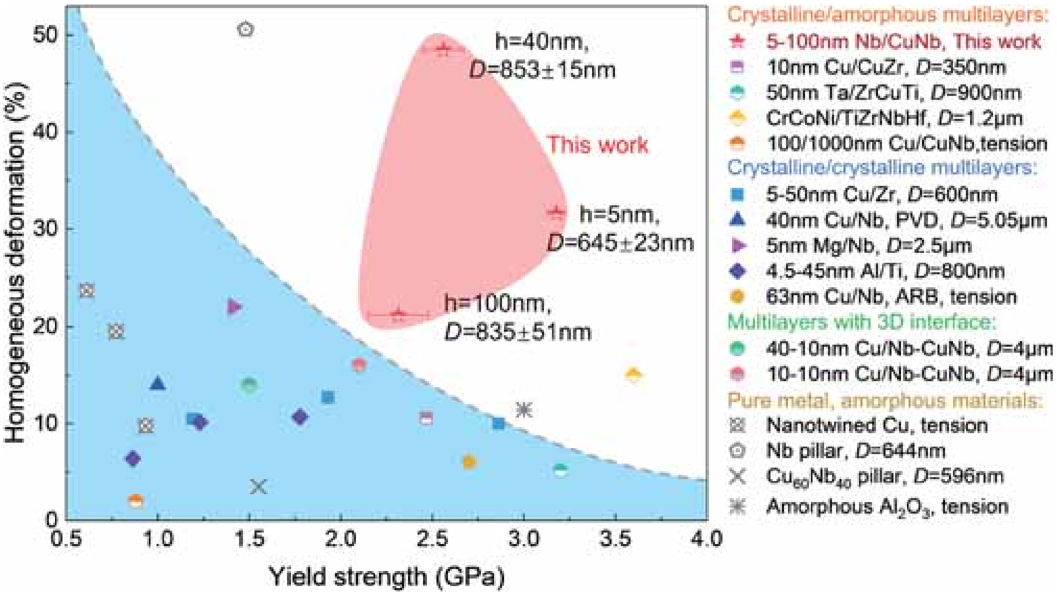

Fig. 22. . The map on the homogeneous deformation (without shear banding and cracking under MC) and yield strength of the Nb/amorphous CuNb NMFs, in comparison with the corresponding data for the constituents (Nb and amorphous CuNb films) and other NMFs including crystalline/amorphous crystalline/amorphous (Chou et al., 2011; Fan et al., 2017b; Wu et al., 2021; Zhang et al., 2012c), crystalline/crystalline multilayers (Ardeljan et al., 2018; Liu et al., 2018; Mara et al., 2010; Zhang et al., 2012a, 2020b), multilayers with 3D interface (Chen et al., 2020c; Cheng et al., 2022)), nanostructured pure metal (Lu et al., 2009) and amorphous material (Frankberg et al., 2019). Note that the tensile uniform elongation for the materials designed by (Frankberg et al., 2019; Liu et al., 2018; Lu et al., 2009) was adopted to be the HDSs for comparison.

the analytical expressions for all the strain components in the shear banding region (region 1) and the region outside the shear banding area (region 0), which are otherwise inaccessible without this assumption. Note that this assumption can be abandoned if the indentation was conducted by spherical indenter, instead of the present Vickers one. Therefore, it is believed that the proposed theoretical model will give more accurate evaluation on the plasticity of NMF samples by using the spherical indenter.

The second assumption is that the trivial strain components in region 0 are ignored considering that the deformation in region 0 is almost homogeneous and is much less than that of region 1. In this case, the effective strain in region 0 can be significantly simplified (Eq. (4)). The third one is that the deformation under indentation is assumed to be small, in order to derive the analytical formulas of the components of circumferential strain ε_θ^1 (Eqs. (7)-(10)) and shear strain γ_{rz}^1 (Eq. (11)) in region 1. All the above assumptions are essential to give an efficient but reliable calculation on the HDS, i.e., $\varepsilon_{\mathrm{HDS}}^{\mathrm{MI}}$, under MIs (Eq. (13)).

4. Conclusions

In this work, systematic MC tests have been conducted to explore the mechanical performances of the BCC Nb/amorphous CuNb NMFs with layer thickness of 100 nm, 40 nm and 5 nm, with the aid of FE and MD simulations. The deformation behaviors of the NMFs under MC-induced isostress state are distinct from those under MI-produced 3-D stress state as discovered in our previous study (Qin et al., 2024). However, both MC and MI tests show that the NMFs exhibit a non-monotonic size-dependent plasticity, achieving the optimal strength-plasticity balance (with a yield strength of 2.56 GPa and a HDS of 48.5 %) in the sample with layer thickness of 40 nm. The further coarsening (to 100 nm) or refining (to 5 nm) of the constituent layers deteriorates the plasticity, i.e., the HDS is decreased down to 21.2 % in the former and 31.6 % in the latter, which are induced by the nano-cracks and shear banding respectively.

The post-TEM analysis on the microstructures of the deformed pillar of the 40 nm sample and the correlated MD simulations clearly show that the homogeneous plastic flow in the amorphous phase and the deformation twinning in the BCC Nb layer are responsible for the excellent plasticity of the 40 nm sample. The formation of nano-cracks in the amorphous phase in the 100 nm sample was attributed to the shear stress produced by the extrusion of the crystalline Nb layer due to the plastic incomparability between the soft crystalline phase and hard amorphous phase. The shear banding in the 5 nm sample was triggered by the strain localization-induced interface broken in the pillar corner and pillar center, as revealed by TEM observations and FE simulations.

An effective strain based-theoretical model has been proposed to quantitatively evaluate the plasticity (represented by the HDS) of the NMFs by incorporating the MI-induced 3-D stress state. The calculated HDSs under MI are in quantitatively agreement with the HDSs measured by MC, i.e., it increases from 14.4 % to 38.4 %, then decreases to 26.9 % for the former, and the corresponding values for the latter are 21.2 %, 48.5 % and 36.1 %. Note that the theoretical model has been made based on several essential assumptions and simplifications. Hence, there might be some limitations in the application of the proposed theoretical model. The model could be improved if the following strategies could be adopted in the future. First, the theoretical model can only provide a quantitative evaluation on the plasticity of NMFs in a first approximation. The accuracy of the predictions could be improved by using spherical indenter and by incorporating large deformation. Second, the accuracy of the predictions will also be enhanced if more MI tests could be conducted to obtain an accurate evaluation for the limit value of the MI-measured homogeneous deformation strain ($\varepsilon_{\mathrm{HDS}}^{\mathrm{MI}}$), i.e., $\varepsilon_{\mathrm{HDS}}^{l}$, for the tested samples. For example, the $\varepsilon_{\mathrm{HDS}}^{l}$ value will increase if the 40 nm sample still shows homogeneous deformation with bigger applied load (larger than 50 gf as used in the present study), in which case the $\varepsilon_{\mathrm{HDS}}^{\mathrm{MI}}$ value also increases. As a result, the discrepancy between the MI-derived HDSs and the MC-measured ones will be definitely reduced.

In summary, this work has made an attempt to give a convenient way to quantitatively evaluate the plasticity of the NMFs by using several simple MI tests with the aid of the newly developed theoretical model, so that the time-consuming and expensive MC tests could be avoided.

CRediT authorship contribution statement

Feng Qin: Investigation, Methodology, Formal analysis, Validation, Writing – original draft. **Yaodong Wang:** Investigation. **Jie Chen:** Investigation. **Shaohua Chen:** Writing – review & editing. **Jianjun Li:** Conceptualization, Methodology, Supervision, Project administration, Supervision, Funding acquisition, Writing – review & editing.

Declaration of competing interest

The authors declare that they have no known competing financial interests or personal relationships that could have appeared to influence the work reported in this paper.

Acknowledgments

This work was supported by the National Natural Science Foundation of China (NSFC) (Grant No. 12272413), the Natural Science Foundation of Hunan Province (Grant No. 2025JJ20010), the Project of State Key Laboratory of Precision Manufacturing for Extreme Service Performance, Central South University (Grant No. ZZYJKT2024-11), and the Opening Fund of State Key Laboratory of Nonlinear Mechanics. The authors appreciate the support for the computational resources for the atomic simulations from the High Performance Computing Center of Central South University.

Supplementary materials

Supplementary material associated with this article can be found, in the online version, at doi:10.1016/j.ijplas.2025.104294.

Data availability

Data will be made available on request.

References

Anderson, P.M., Bingert, J.F., Misra, A., Hirth, J.P., 2003. Rolling textures in nanoscale Cu/Nb multilayers. Acta Mater. 51, 6059–6075. https://doi.org/10.1016/S1359-6454(03)00428-2.

Ardeljan, M., Knezevic, M., Jain, M., Pathak, S., Kumar, A., Li, N., Mara, N.A., Baldwin, J.K., Beyerlein, I.J., 2018. Room temperature deformation mechanisms of Mg/Nb nanolayered composites. J. Mater. Res. 33, 1311–1332. https://doi.org/10.1557/jmr.2018.107.

Beyerlein, I.J., Mara, N.A., Wang, J., Carpenter, J.S., Zheng, S.J., Han, W.Z., Zhang, R.F., Kang, K., Nizolek, T., Pollock, T.M., 2012. Structure–property–functionality of bimetal interfaces. JOM 64, 1192–1207. https://doi.org/10.1007/s11837-012-0431-0.

Bitzek, E., Derlet, P.M., Anderson, P.M., Van Swygenhoven, H., 2008. The stress–strain response of nanocrystalline metals: a statistical analysis of atomistic simulations. Acta Mater. 56, 4846–4857. https://doi.org/10.1016/j.actamat.2008.05.043.

Bristowe, P.D., Crocker, A.G., 1975. A computer simulation study of the structures of twin boundaries in body-centred cubic crystals. Philos. Mag. 31, 503–517. https://doi.org/10.1080/14786437508226533.

Cao, Z.H., Cai, Y.P., Sun, C., Ma, Y.J., Wei, M.Z., Li, Q., Lu, H.M., Wang, H., Zhang, X., Meng, X.K., 2019. Tailoring strength and plasticity of Ag/Nb nanolaminates via intrinsic microstructure and extrinsic dimension. Int. J. Plast. 113, 145–157. https://doi.org/10.1016/j.ijplas.2018.09.012.

Cao, Z.H., Zhai, G.Y., Ma, Y.J., Ding, L.P., Li, P.F., Liu, H.L., Lu, H.M., Cai, Y.P., Wang, G.J., Meng, X.K., 2021. Evolution of interfacial character and its influence on strain hardening in dual-phase high entropy alloys at nanoscale. Int. J. Plast. 145, 103081. https://doi.org/10.1016/j.ijplas.2021.103081.

Chawla, N., Singh, D.R.P., Shen, Y.L., Tang, G., Chawla, K.K., 2008. Indentation mechanics and fracture behavior of metal/ceramic nanolaminate composites. J. Mater. Sci. 43, 4383–4390. https://doi.org/10.1007/s10853-008-2450-3.

Chen, C.Q., Pei, Y.T., De Hosson, J.T.M., 2010. Effects of size on the mechanical response of metallic glasses investigated through in situ TEM bending and compression experiments. Acta Mater. 58, 189–200. https://doi.org/10.1016/j.actamat.2009.08.070.

Chen, H.H., Zhao, Y.F., Zhang, J.Y., Wang, Y.Q., Li, G.Y., Wu, K., Liu, G., Sun, J., 2020a. He-ion irradiation effects on the microstructure stability and size-dependent mechanical behavior of high entropy alloy/Cu nanotwinned nanolaminates. Int. J. Plast. 133, 102839. https://doi.org/10.1016/j.ijplas.2020.102839.

Chen, T., Yuan, R., Beyerlein, I.J., Zhou, C., 2020b. Predicting the size scaling in strength of nanolayered materials by a discrete slip crystal plasticity model. Int. J. Plast. 124, 247–260. https://doi.org/10.1016/j.ijplas.2019.08.016.

Chen, Y., Jiang, M.Q., Dai, L.H., 2013. Collective evolution dynamics of multiple shear bands in bulk metallic glasses. Int. J. Plast. 50, 18–36. https://doi.org/10.1016/j.ijplas.2013.03.010.

Chen, Y., Li, N., Hoagland, R.G., Liu, X.Y., Baldwin, J.K., Beyerlein, I.J., Cheng, J.Y., Mara, N.A., 2020c. Effects of three-dimensional Cu/Nb interfaces on strengthening and shear banding in nanoscale metallic multilayers. Acta Mater. 199, 593–601. https://doi.org/10.1016/j.actamat.2020.08.019.

Cheng, B., Trelewicz, J.R., 2016. Mechanistic coupling of dislocation and shear transformation zone plasticity in crystalline-amorphous nanolaminates. Acta Mater. 117, 293–305. https://doi.org/10.1016/j.actamat.2016.07.011.

Cheng, J.Y., Wang, J., Chen, Y., Xu, S., Barriocanal, J.G., Baldwin, J.K., Beyerlein, I.J., Mara, N.A., 2024. 3D interfaces enhance nanolaminate strength and deformability in multiple loading orientations. Acta Mater. 267, 119697. https://doi.org/10.1016/j.actamat.2024.119697.

Cheng, J.Y., Xu, S., Chen, Y., Li, Z., Baldwin, J.K., Beyerlein, I.J., Mara, N.A., 2022. Simultaneous high-strength and deformable nanolaminates with thick biphase interfaces. Nano Lett. 22, 1897–1904. https://doi.org/10.1021/acs.nanolett.1c04144.

Chou, H.S., Du, X.H., Lee, C.J., Huang, J.C., 2011. Enhanced mechanical properties of multilayered micropillars of amorphous ZrCuTi and nanocrystalline Ta layers. Intermetallics 19, 1047–1051. https://doi.org/10.1016/j.intermet.2011.03.015.

Conner, R.D., Johnson, W.L., Paton, N.E., Nix, W.D., 2003. Shear bands and cracking of metallic glass plates in bending. J. Appl. Phys. 94, 904–911. https://doi.org/10.1063/1.1582555.

Cruzado, A., Gan, B., Jiménez, M., Barba, D., Ostolaza, K., Linaza, A., Molina-Aldareguia, J.M., Llorca, J., Segurado, J., 2015. Multiscale modeling of the mechanical behavior of IN718 superalloy based on micropillar compression and computational homogenization. Acta Mater. 98, 242–253. https://doi.org/10.1016/j.actamat.2015.07.006.

Cui, Y., Huang, P., Wang, F., Lu, T.J., Xu, K.W., 2015. The hardness and related deformation mechanisms in nanoscale crystalline–amorphous multilayers. Thin Solid Films 584, 270–276. https://doi.org/10.1016/j.tsf.2015.01.067.

Dehm, G., Jaya, B.N., Raghavan, R., Kirchlechner, C., 2018. Overview on micro- and nanomechanical testing: new insights in interface plasticity and fracture at small length scales. Acta Mater. 142, 248–282. https://doi.org/10.1016/j.actamat.2017.06.019.

Dong, S., Chen, T., Huang, S., Li, N., Zhou, C., 2020. Thickness-dependent shear localization in Cu/Nb metallic nanolayered composites. Scr. Mater. 187, 323–328. https://doi.org/10.1016/j.scriptamat.2020.06.049.

Faisal, A.H.M., Weinberger, C.R., 2023. Nucleation of extended defects in BCC transition metals. Int. J. Plast. 170, 103742. https://doi.org/10.1016/j.ijplas.2023.103742.

Fan, Z., Li, J., Yang, Y., Wang, J., Li, Q., Xue, S., Wang, H., Lou, J., Zhang, X., 2017a. "Ductile" fracture of metallic glass nanolaminates. Adv. Mater. Interfaces 4, 1700510. https://doi.org/10.1002/admi.201700510.

Fan, Z., Li, Q., Li, J., Xue, S., Wang, H., Zhang, X., 2017b. Tailoring plasticity of metallic glasses via interfaces in Cu/amorphous CuNb laminates. J. Mater. Res. 32, 2680–2689. https://doi.org/10.1557/jmr.2017.249.

Fan, Z., Xue, S., Wang, J., Yu, K.Y., Wang, H., Zhang, X., 2016. Unusual size dependent strengthening mechanisms of Cu/amorphous CuNb multilayers. Acta Mater. 120, 327–336. https://doi.org/10.1016/j.actamat.2016.08.064.

Feng, X.B., Zhang, J.Y., Wang, Y.Q., Hou, Z.Q., Wu, K., Liu, G., Sun, J., 2017. Size effects on the mechanical properties of nanocrystalline NbMoTaW refractory high entropy alloy thin films. Int. J. Plast. 95, 264–277. https://doi.org/10.1016/j.ijplas.2017.04.013.

Frankberg, E.J., Kalikka, J., García Ferré, F., Joly-Pottuz, L., Salminen, T., Hintikka, J., Hokka, M., Koneti, S., Douillard, T., Le Saint, B., Kreiml, P., Cordill, M.J., Epicier, T., Stauffer, D., Vanazzi, M., Roiban, L., Akola, J., Di Fonzo, F., Levänen, E., Masenelli-Varlot, K., 2019. Highly ductile amorphous oxide at room temperature and high strain rate. Science 366, 864–869. https://doi.org/10.1126/science.aav1254.

Frick, C.P., Clark, B.G., Orso, S., Schneider, A.S., Arzt, E., 2008. Size effect on strength and strain hardening of small-scale [111]nickel compression pillars. Mater. Sci. Eng. A 489, 319–329. https://doi.org/10.1016/j.msea.2007.12.038.

Gan, L., Ben-Nissan, B., Ben-David, A., 1996. Modelling and finite element analysis of ultra-microhardness indentation of thin films. Thin Solid Films 290, 362–366. https://doi.org/10.1016/S0040-6090(96)08972-9.

Gram, M.D., Carpenter, J.S., Anderson, P.M., 2015. An indentation-based method to determine constituent strengths within nanolayered composites. Acta Mater. 92, 255–264. https://doi.org/10.1016/j.actamat.2015.04.002.

Greer, A.L., Cheng, Y.Q., Ma, E., 2013. Shear bands in metallic glasses. Mater. Sci. Eng. R 74, 71–132. https://doi.org/10.1016/j.mser.2013.04.001.

Greer, J.R., De Hosson, J.T.M., 2011. Plasticity in small-sized metallic systems: intrinsic versus extrinsic size effect. Prog. Mater. Sci. 56, 654–724. https://doi.org/10.1016/j.pmatsci.2011.01.005.

Greer, J.R., Oliver, W.C., Nix, W.D., 2005. Size dependence of mechanical properties of gold at the micron scale in the absence of strain gradients. Acta Mater. 53, 1821–1830. https://doi.org/10.1016/j.actamat.2004.12.031.

Gu, C., Wang, F., Huang, P., Xu, K.W., Lu, T.J., 2017. Size-dependent hardness and tensile plasticity of Ta-Zr 61 Cu 17.5 Ni 10 Al l7.5 Si 4 nanolaminates. J. Alloys Compd. 707, 321–326. https://doi.org/10.1016/j.jallcom.2016.11.156.

Guo, H., Yan, P.F., Wang, Y.B., Tan, J., Zhang, Z.F., Sui, M.L., Ma, E., 2007. Tensile ductility and necking of metallic glass. Nat. Mater. 6, 735. https://doi.org/10.1038/nmat1984.

Guo, W., Jägle, E., Yao, J., Maier, V., Korte-Kerzel, S., Schneider, J.M., Raabe, D., 2014. Intrinsic and extrinsic size effects in the deformation of amorphous CuZr/nanocrystalline Cu nanolaminates. Acta Mater. 80, 94–106. https://doi.org/10.1016/j.actamat.2014.07.027.

Guo, W., Yao, J., Jägle, E.A., Choi, P.-P., Herbig, M., Schneider, J.M., Raabe, D., 2015. Deformation induced alloying in crystalline – metallic glass nano-composites. Mater. Sci. Eng.: A 628, 269–280. https://doi.org/10.1016/j.msea.2015.01.062.

Ham, B., Zhang, X., 2011. High strength Mg/Nb nanolayer composites. Mater. Sci. Eng. A 528, 2028–2033. https://doi.org/10.1016/j.msea.2010.10.101.

Hemker, K.J., Sharpe, W.N., 2007. Microscale characterization of mechanical properties. Annu. Rev. Mater. Res. 37, 93–126. https://doi.org/10.1146/annurev.matsci.36.062705.134551.

Hopcroft, M.A., Nix, W.D., Kenny, T.W., 2010. What is the Young's modulus of silicon? J. Microelectromech. Syst. 19, 229–238. https://doi.org/10.1109/JMEMS.2009.2039697.

Jang, D., Greer, J.R., 2010. Transition from a strong-yet-brittle to a stronger-and-ductile state by size reduction of metallic glasses. Nat. Mater. 9, 215–219. https://doi.org/10.1038/nmat2622.

Jang, D., Gross, C.T., Greer, J.R., 2011. Effects of size on the strength and deformation mechanism in Zr-based metallic glasses. Int. J. Plast. 27, 858–867. https://doi.org/10.1016/j.ijplas.2010.09.010.

Jian, W.-R., Xu, S., Su, Y., Beyerlein, I.J., 2022. Role of layer thickness and dislocation distribution in confined layer slip in nanolaminated Nb. Int. J. Plast. 152, 103239. https://doi.org/10.1016/j.ijplas.2022.103239.

Jiang, B., Tu, A., Wang, H., Duan, H., He, S., Ye, H., Du, K., 2018. Direct observation of deformation twinning under stress gradient in body-centered cubic metals. Acta Mater. 155, 56–68. https://doi.org/10.1016/j.actamat.2018.05.061.

Jiang, M.Q., Dai, L.H., 2009. On the origin of shear banding instability in metallic glasses. J. Mech. Phys. Solids 57, 1267–1292. https://doi.org/10.1016/j.jmps.2009.04.008.

Jiang, S.S., Gan, K.F., Huang, Y.J., Xue, P., Ning, Z.L., Sun, J.F., Ngan, A.H.W., 2020. Stochastic deformation and shear transformation zones of the glassy matrix in CuZr-based metallic-glass composites. Int. J. Plast. 125, 52–62. https://doi.org/10.1016/j.ijplas.2019.09.005.

Kim, J.-Y., Jang, D., Greer, J.R., 2009. Insight into the deformation behavior of niobium single crystals under uniaxial compression and tension at the nanoscale. Scr. Mater. 61, 300–303. https://doi.org/10.1016/j.scriptamat.2009.04.012.

Kim, J.-Y., Jang, D., Greer, J.R., 2011. Nanolaminates utilizing size-dependent homogeneous plasticity of metallic glasses. Adv. Funct. Mater. 21, 4550–4554. https://doi.org/10.1002/adfm.201101164.

Knorr, I., Cordero, N.M., Lilleodden, E.T., Volkert, C.A., 2013. Mechanical behavior of nanoscale Cu/PdSi multilayers. Acta Mater. 61, 4984–4995. https://doi.org/10.1016/j.actamat.2013.04.047.

Kou, H., Lu, J., Li, Y., 2014. High-strength and high-ductility nanostructured and amorphous metallic materials. Adv. Mater. 26, 5518–5524. https://doi.org/10.1002/adma.201401595.

Lee, S., Cho, H., Bronkhorst, C.A., Pokharel, R., Brown, D.W., Clausen, B., Vogel, S.C., Anghel, V., Gray, G.T., Mayeur, J.R., 2023. Deformation, dislocation evolution and the non-Schmid effect in body-centered-cubic single- and polycrystal tantalum. Int. J. Plast. 163, 103529. https://doi.org/10.1016/j.ijplas.2023.103529.

Lee, W.B., Chen, Y.P., 2010. Simulation of micro-indentation hardness of FCC single crystals by mechanism-based strain gradient crystal plasticity. Int. J. Plast. 26, 1527–1540. https://doi.org/10.1016/j.ijplas.2010.01.011.

Li, J., Chen, Y., Xue, S., Wang, H., Zhang, X., 2016. Comparison of size dependent strengthening mechanisms in Ag/Fe and Ag/Ni multilayers. Acta Mater. 114, 154–163. https://doi.org/10.1016/j.actamat.2016.05.030.

Li, J., Lu, W., Gibson, J., Zhang, S., Chen, T., Korte-Kerzel, S., Raabe, D., 2018. Eliminating deformation incompatibility in composites by gradient nanolayer architectures. Sci. Rep. 8, 16216. https://doi.org/10.1038/s41598-018-34369-9.

Li, J., Lu, W., Gibson, J., Zhang, S., Korte-Kerzel, S., Raabe, D., 2020. Compatible deformation and extra strengthening by heterogeneous nanolayer composites. Scr. Mater. 179, 30–35. https://doi.org/10.1016/j.scriptamat.2020.01.006.

Li, J., Lu, W., Zhang, S., Raabe, D., 2017. Large strain synergetic material deformation enabled by hybrid nanolayer architectures. Sci. Rep. 7, 11371. https://doi.org/10.1038/s41598-017-11001-w.

Li, J., Qin, F., Yan, D., Lu, W., Yao, J., 2022. Shear instability in heterogeneous nanolayered Cu/Zr composites. J. Mater. Sci. Technol. 105, 81–91. https://doi.org/10.1016/j.jmst.2021.06.070.

Li, L., Anderson, P.M., Lee, M.-G., Bitzek, E., Derlet, P., Swygenhoven, H.V., 2009. The stress–strain response of nanocrystalline metals: a quantized crystal plasticity approach. Acta Mater. 57, 812–822. https://doi.org/10.1016/j.actamat.2008.10.035.

Li, M., Zhou, Y., Wang, P., Malomo, B., Yang, L., 2023. Structural mechanisms of enhanced mechanical property in ZrCu metallic glass at low temperatures. Int. J. Plast. 167, 103680. https://doi.org/10.1016/j.ijplas.2023.103680.

Li, N., Wang, J., Misra, A., Huang, J.Y., 2012. Direct Observations of Confined Layer Slip in Cu/Nb Multilayers. Microsc. Microanal. 18, 1155–1162. https://doi.org/10.1017/S143192761200133X.

Li, S., Ding, X., Deng, J., Lookman, T., Li, J., Ren, X., Sun, J., Saxena, A., 2010a. Superelasticity in bcc nanowires by a reversible twinning mechanism. Phys. Rev. B 82, 205435. https://doi.org/10.1103/PhysRevB.82.205435.

Li, Y.P., Tan, J., Zhang, G.P., 2008. Interface instability within shear bands in nanoscale Au/Cu multilayers. Scr. Mater. 59, 1226–1229. https://doi.org/10.1016/j.scriptamat.2008.08.017.

Li, Y.P., Zhu, X.F., Tan, J., Wu, B., Wang, W., Zhang, G.P., 2011. Comparative investigation of strength and plastic instability in Cu/Au and Cu/Cr multilayers by indentation. J. Mater. Res. 24, 728–735. https://doi.org/10.1557/jmr.2009.0092.

Li, Y.P., Zhu, X.F., Zhang, G.P., Tan, J., Wang, W., Wu, B., 2010b. Investigation of deformation instability of Au/Cu multilayers by indentation. Philos. Mag. 90, 3049–3067. https://doi.org/10.1080/14786431003776802.

Liang, F., Wang, Z., Li, M., Zhang, B., Luo, X., Zhu, X., Zhang, G., 2024. Exceptional ductility through interface-constrained grain growth for the ultrafine-scale Ni/Ni-W layered composites. Int. J. Plast. 176, 103959. https://doi.org/10.1016/j.ijplas.2024.103959.

Lim, H., Carroll, J.D., Michael, J.R., Battaile, C.C., Chen, S.R., Lane D., J.M., 2020. Investigating active slip planes in tantalum under compressive load: crystal plasticity and slip trace analyses of single crystals. Acta Mater. 185, 1–12. https://doi.org/10.1016/j.actamat.2019.11.030.

Liu, Y., Chen, Y., Yu, K.Y., Wang, H., Chen, J., Zhang, X., 2013. Stacking fault and partial dislocation dominated strengthening mechanisms in highly textured Cu/Co multilayers. Int. J. Plast. 49, 152–163. https://doi.org/10.1016/j.ijplas.2013.03.005.

Liu, Z., Monclús, M.A., Yang, L.W., Castillo-Rodríguez, M., Molina-Aldareguía, J.M., Llorca, J., 2018. Tensile deformation and fracture mechanisms of Cu/Nb nanolaminates studied by in situ TEM mechanical tests. Extreme Mech. Lett. 25, 60–65. https://doi.org/10.1016/j.eml.2018.10.007.

Lotfian, S., Rodríguez, M., Yazzie, K.E., Chawla, N., Llorca, J., Molina-Aldareguía, J.M., 2013. High temperature micropillar compression of Al/SiC nanolaminates. Acta Mater. 61, 4439–4451. https://doi.org/10.1016/j.actamat.2013.04.013.

Lu, L., Chen, X., Huang, X., Lu, K., 2009. Revealing the maximum strength in nanotwinned copper. Science 323, 607–610. https://doi.org/10.1126/science.1167641.

Lyu, H., Hamid, M., Ruimi, A., Zbib, H.M., 2017. Stress/strain gradient plasticity model for size effects in heterogeneous nano-microstructures. Int. J. Plast. 97, 46–63. https://doi.org/10.1016/j.ijplas.2017.05.009.

Ma, E., Zhu, T., 2017. Towards strength–ductility synergy through the design of heterogeneous nanostructures in metals. Mater. Today 20, 323–331. https://doi.org/10.1016/j.mattod.2017.02.003.

Mara, N.A., Bhattacharyya, D., Hirth, J.P., Dickerson, P., Misra, A., 2010. Mechanism for shear banding in nanolayered composites. Appl. Phys. Lett. 97, 021909. https://doi.org/10.1063/1.3458000.

Mayer, C.R., Yang, L.W., Singh, S.S., Llorca, J., Molina-Aldareguia, J.M., Shen, Y.L., Chawla, N., 2016. Anisotropy, size, and aspect ratio effects on micropillar compression of AlSiC nanolaminate composites. Acta Mater. 114, 25–32. https://doi.org/10.1016/j.actamat.2016.05.018.

Meyers, M.A., Mishra, A., Benson, D.J., 2006. Mechanical properties of nanocrystalline materials. Prog. Mater. Sci. 51, 427–556. https://doi.org/10.1016/j.pmatsci.2005.08.003.

Misra, A., Hirth, J.P., Hoagland, R.G., 2005. Length-scale-dependent deformation mechanisms in incoherent metallic multilayered composites. Acta Mater. 53, 4817–4824. https://doi.org/10.1016/j.actamat.2005.06.025.

Ovid'ko, I.A., Valiev, R.Z., Zhu, Y.T., 2018. Review on superior strength and enhanced ductility of metallic nanomaterials. Prog. Mater. Sci. 94, 462–540. https://doi.org/10.1016/j.pmatsci.2018.02.002.

Qin, F., Chen, F., Hou, J., Lu, W., Chen, S., Li, J., 2024. Strong resistance to shear instability in multilayered metallic composites by nanoscale amorphous-BCC crystalline interfaces. Mater. Sci. Eng. A 891, 145919. https://doi.org/10.1016/j.msea.2023.145919.

Rajagopalan, J., Han Jong, H., Saif, M.T.A., 2007. Plastic deformation recovery in freestanding nanocrystalline aluminum and gold thin films. Science 315, 1831–1834. https://doi.org/10.1126/science.1137580.

Ravichandran, G., Molinari, A., 2005. Analysis of shear banding in metallic glasses under bending. Acta Mater. 53, 4087–4095. https://doi.org/10.1016/j.actamat.2005.05.011.

Russell, K., Killeen, C., Peter, N.J., Schwaiger, R., Trelewicz, J.R., Hodge, A.M., 2024. Microstructure and thermal stability of crystalline/amorphous Fe/FeW nanomultilayers. Scr. Mater. 242, 115962. https://doi.org/10.1016/j.scriptamat.2023.115962.

Schiøtz, J., Jacobsen, K.W., 2003. A maximum in the strength of nanocrystalline copper. Science 301, 1357–1359. https://doi.org/10.1126/science.1086636.

Schuh, C., Hufnagel, T., Ramamurty, U., 2007. Mechanical behavior of amorphous alloys. Acta Mater. 55, 4067–4109. https://doi.org/10.1016/j.actamat.2007.01.052.

Schuler, J.D., Grigorian, C.M., Barr, C.M., Boyce, B.L., Hattar, K., Rupert, T.J., 2020. Amorphous intergranular films mitigate radiation damage in nanocrystalline Cu-Zr. Acta Mater. 186, 341–354. https://doi.org/10.1016/j.actamat.2019.12.048.

Sha, Z.-D., Branicio, P.S., Lee, H.P., Tay, T.E., 2017. Strong and ductile nanolaminate composites combining metallic glasses and nanoglasses. Int. J. Plast. 90, 231–241. https://doi.org/10.1016/j.ijplas.2017.01.010.

Shan, Z.W., Mishra, R.K., Syed Asif, S.A., Warren, O.L., Minor, A.M., 2008. Mechanical annealing and source-limited deformation in submicrometre-diameter Ni crystals. Nat. Mater. 7, 115–119. https://doi.org/10.1038/nmat2085.

Singh, D.R.P., Chawla, N., Tang, G., Shen, Y.L., 2010. Micropillar compression of Al/SiC nanolaminates. Acta Mater. 58, 6628–6636. https://doi.org/10.1016/j.actamat.2010.08.025.

Singh, D.R.P., Chawla, N., Tang, G., Shen, Y.L., 2011. Anomalous viscoplasticity during nanoindentation of Al/SiC nanolaminated composites. Mater. Sci. Eng. A 528, 4608–4614. https://doi.org/10.1016/j.msea.2011.02.058.

Spear, K.E., Dismukes, J.P., 1994. Synthetic Diamond: Emerging CVD Science and Technology. John Wiley & Sons, New York.

Su, R., Neffati, D., Li, Q., Xue, S., Fan, C., Cho, J., Zhang, Y., Li, J., Wang, H., Kulkarni, Y., Zhang, X., 2021. Ultra-high strength and plasticity mediated by partial dislocations and defect networks: part II: layer thickness effect. Acta Mater. 204. https://doi.org/10.1016/j.actamat.2020.116494.

Tang, G., Shen, Y.L., Singh, D.R.P., Chawla, N., 2010. Indentation behavior of metal–ceramic multilayers at the nanoscale: numerical analysis and experimental verification. Acta Mater. 58, 2033–2044. https://doi.org/10.1016/j.actamat.2009.11.046.

Uchic, M.D., Dimiduk, D.M., Florando, J.N., Nix, W.D., 2004. Sample dimensions influence strength and crystal plasticity. Science 305, 986–989. https://doi.org/10.1126/science.1098993.

Uchic, M.D., Shade, P.A., Dimiduk, D.M., 2009. Plasticity of micrometer-scale single crystals in compression. Annu. Rev. Mater. Res. 39, 361–386. https://doi.org/10.1146/annurev-matsci-082908-145422.

Van Swygenhoven, H., Derlet, P.M., Frøseth, A.G., 2006. Nucleation and propagation of dislocations in nanocrystalline fcc metals. Acta Mater. 54, 1975–1983. https://doi.org/10.1016/j.actamat.2005.12.026.

Vítek, V., 1970. Multilayer stacking faults and twins on {211} planes in B.C.C. metals. Scr. Metall. 4, 725–732. https://doi.org/10.1016/0036-9748(70)90214-0.

Vo, N.Q., Averback, R.S., Ashkenazy, Y., Bellon, P., Wang, J., 2012. Forced chemical mixing at Cu-Nb interfaces under severe plastic deformation. J. Mater. Res. 27, 1621–1630. https://doi.org/10.1557/jmr.2012.106.

Volkert, C.A., Lilleodden, E.T., 2006. Size effects in the deformation of sub-micron Au columns. Philos. Mag. 86, 5567–5579. https://doi.org/10.1080/14786430600567739.

Wang, F., Huang, P., Xu, M., Lu, T.J., Xu, K.W., 2011. Shear banding deformation in Cu/Ta nano-multilayers. Mater. Sci. Eng. A 528, 7290–7294. https://doi.org/10.1016/j.msea.2011.06.019.

Wang, J., Faisal, A.H.M., Li, X., Hong, Y., Zhu, Q., Bei, H., Zhang, Z., Mao, S.X., Weinberger, C.R., 2022. Discrete twinning dynamics and size-dependent dislocation-to twin transition in body-centred cubic tungsten. J. Mater. Sci. Technol. 106, 33–40. https://doi.org/10.1016/j.jmst.2021.08.010.

Wang, Y., Huang, C., Ma, X., Zhao, J., Guo, F., Fang, X., Zhu, Y., Wei, Y., 2023. The optimum grain size for strength-ductility combination in metals. Int. J. Plast. 164, 103574. https://doi.org/10.1016/j.ijplas.2023.103574.

Wang, Y., Kiener, D., Liang, X., Bian, J., Wu, K., Zhang, J., Liu, G., Sun, J., 2018. Constituent constraining effects on the microstructural evolution, ductility, and fracture mode of crystalline/amorphous nanolaminates. J. Alloys Compd. 768, 88–96. https://doi.org/10.1016/j.jallcom.2018.07.177.

Wang, Y., Li, J., Li, J., Chen, S., 2024. On the strain delocalization mechanism of Cu/Nb nanolayered composites with amorphous interfacial layers. Int. J. Plast. 172, 103856. https://doi.org/10.1016/j.ijplas.2023.103856.

Wang, Y.M., Li, J., Hamza, A.V., Barbee, T.W., 2007. Ductile crystalline–amorphous nanolaminates. Proc. Natl. Acad. Sci. U.S.A. 104, 11155–11160. https://doi.org/10.1073/pnas.070234410.

Wang, Y.Q., Zhang, J.Y., Liang, X.Q., Wu, K., Liu, G., Sun, J., 2015. Size- and constituent-dependent deformation mechanisms and strain rate sensitivity in nanolaminated crystalline Cu/amorphous Cu–Zr films. Acta Mater. 95, 132–144. https://doi.org/10.1016/j.actamat.2015.05.007.

Weinberger, C.R., Boyce, B.L., Battaile, C.C., 2013. Slip planes in bcc transition metals. Int. Mater. Rev. 58, 296–314. https://doi.org/10.1179/1743280412Y.0000000015.

Wen, S.P., Zong, R.L., Zeng, F., Gao, Y., Pan, F., 2007. Nanoindentation investigation of the mechanical behaviors of nanoscale Ag/Cu multilayers. J. Mater. Res. 22, 3423–3431. https://doi.org/10.1557/JMR.2007.0423.

Wen, T., Liu, A., Wang, R., Zhang, L., Han, J., Wang, H., Srolovitz, D.J., Wu, Z., 2023. Modelling of dislocations, twins and crack-tips in HCP and BCC Ti. Int. J. Plast. 166, 103644. https://doi.org/10.1016/j.ijplas.2023.103644.

Wu, G., Balachandran, S., Gault, B., Xia, W., Liu, C., Rao, Z., Wei, Y., Liu, S., Lu, J., Herbig, M., Lu, W., Dehm, G., Li, Z., Raabe, D., 2020. Crystal-glass high-entropy nanocomposites with near theoretical compressive strength and large deformability. Adv. Mater. 32, e2002619. https://doi.org/10.1002/adma.202002619.

Wu, G., Liu, C., Brognara, A., Ghidelli, M., Bao, Y., Liu, S., Wu, X., Xia, W., Zhao, H., Rao, J., Ponge, D., Devulapalli, V., Lu, W., Dehm, G., Raabe, D., Li, Z., 2021. Symbiotic crystal-glass alloys via dynamic chemical partitioning. Mater. Today 51, 6–14. https://doi.org/10.1016/j.mattod.2021.10.025.

Wu, G., Liu, C., Yan, Y.-Q., Liu, S., Ma, X., Yue, S., Shan, Z.-W., 2024. Elemental partitioning-mediated crystalline-to-amorphous phase transformation under quasi-static deformation. Nat. Commun. 15, 1223. https://doi.org/10.1038/s41467-024-45513-7.

Wu, G., Liu, S., Wang, Q., Rao, J., Xia, W., Yan, Y.-Q., Eckert, J., Liu, C., Ma, E., Shan, Z.-W., 2023a. Substantially enhanced homogeneous plastic flow in hierarchically nanodomained amorphous alloys. Nat. Commun. 14, 3670. https://doi.org/10.1038/s41467-023-39296-6.

Wu, H., Fan, G., 2020. An overview of tailoring strain delocalization for strength-ductility synergy. Prog. Mater. Sci. 113, 100675. https://doi.org/10.1016/j.pmatsci.2020.100675.

Wu, H., Huang, M., Xia, Y., Li, X., Li, R., Liu, C., Gan, W., Xiao, T., Geng, L., Liu, Q., Fan, G., 2023b. The importance of interfacial stress-affected zone in evading the strength-ductility trade-off of heterogeneous multi-layered composites. Int. J. Plast. 160, 103485. https://doi.org/10.1016/j.ijplas.2022.103485.

Yoo, B.-G., Kim, J.-Y., Kim, Y.-J., Choi, I.-C., Shim, S., Tsui, T.Y., Bei, H., Ramamurty, U., Jang, J.-i., 2012. Increased time-dependent room temperature plasticity in metallic glass nanopillars and its size-dependency. Int. J. Plast. 37, 108–118. https://doi.org/10.1016/j.ijplas.2012.04.005.

Yuan, S., Branicio, P.S., 2020. Gradient microstructure induced shear band constraint, delocalization, and delayed failure in CuZr nanoglasses. Int. J. Plast. 134. https://doi.org/10.1016/j.ijplas.2020.102845.

Zhang, C., Firestein, K.L., Fernando, J.F.S., Siriwardena, D., von Treifeldt, J.E., Golberg, D., 2020a. Recent progress of in situ transmission electron microscopy for energy materials. Adv. Mater. 32, 1904094. https://doi.org/10.1002/adma.201904094.

Zhang, J.Y., Lei, S., Liu, Y., Niu, J.J., Chen, Y., Liu, G., Zhang, X., Sun, J., 2012a. Length scale-dependent deformation behavior of nanolayered Cu/Zr micropillars. Acta Mater. 60, 1610–1622. https://doi.org/10.1016/j.actamat.2011.12.001.

Zhang, J.Y., Lei, S., Niu, J., Liu, Y., Liu, G., Zhang, X., Sun, J., 2012b. Intrinsic and extrinsic size effects on deformation in nanolayered Cu/Zr micropillars: from bulk-like to small-volume materials behavior. Acta Mater. 60, 4054–4064. https://doi.org/10.1016/j.actamat.2012.03.056.

Zhang, J.Y., Liu, G., Lei, S.Y., Niu, J.J., Sun, J., 2012c. Transition from homogeneous-like to shear-band deformation in nanolayered crystalline Cu/amorphous Cu–Zr micropillars: intrinsic vs. extrinsic size effect. Acta Mater. 60, 7183–7196. https://doi.org/10.1016/j.actamat.2012.09.027.

Zhang, Y., Nizolek, T.J., Capolungo, L., Li, N., Carpenter, J.S., McCabe, R.J., 2024. Strong interfaces: the key to high strength in nano metallic laminates. Acta Mater. 280, 120298. https://doi.org/10.1016/j.actamat.2024.120298.

Zhang, Y.F., Li, Q., Gong, M., Xue, S., Ding, J., Li, J., Cho, J., Niu, T., Su, R., Richter, N.A., Wang, H., Wang, J., Zhang, X., 2020b. Deformation behavior and phase transformation of nanotwinned Al/Ti multilayers. Appl. Surf. Sci. 527, 146776. https://doi.org/10.1016/j.apsusc.2020.146776.

Zhao, L., Chen, G., Zheng, H., Jia, S., Li, K., Jiang, R., Li, L., Zhang, Y., Peng, H., Zhao, P., Huang, Z., Wang, J., 2023. Strong size effect on deformation twin-mediated plasticity in body-centered-cubic iron. J. Mater. Sci. Technol. 144, 235–242. https://doi.org/10.1016/j.jmst.2022.11.004.

Zhou, H.F., Zhong, C., Cao, Q.P., Qu, S.X., Wang, X.D., Yang, W., Jiang, J.Z., 2014. Non-localized deformation in metallic alloys with amorphous structure. Acta Mater. 68, 32–41. https://doi.org/10.1016/j.actamat.2014.01.003.

Zou, Y., Ma, H., Spolenak, R., 2015. Ultrastrong ductile and stable high-entropy alloys at small scales. Nat. Commun. 6, 7748. https://doi.org/10.1038/ncomms8748.